Single-cell transcriptomics reveals heterogenous thymic dendritic cell subsets with distinct functions and requirements for thymocyte-regulated crosstalk

Jayashree Srinivasan[1], Bryan R. Helm[2], Yilin Yang[3], Colin Moore[1], John F. Moore[1], Aparna Calindi[1], Hilary J Selden[1], Cody N. Heiser[4], Qi Liu[2], Ken S. Lau[3], Lauren I. R. Ehrlich[1,5,6*]

[1]Department of Molecular Biosciences, The University of Texas at Austin, Austin, TX 78712, USA
[2]Department of Biostatistics, Vanderbilt University Medical Center, Nashville, TN 37232, USA
[3]Department of Cell and Developmental Biology, Vanderbilt University School of Medicine, Nashville, TN 37232, USA
[4]Program in Chemical and Physical Biology, Vanderbilt University School of Medicine, Nashville, TN 37232, USA
[5]Department of Oncology, Livestrong Cancer Institutes, Dell Medical School, The University of Texas at Austin, Austin, TX 78712, USA
[6]Lead Contact
[*]Correspondence: lehrlich@austin.utexas.edu

SUMMARY

Dendritic cells (DCs) are essential for establishing central tolerance in the thymus; however, mechanisms supporting their homeostasis and activation remain unresolved. Through single-cell transcriptomics and functional assays, we identify seven thymic conventional DC (cDC) subsets and discriminate their abilities to present self-antigens and induce regulatory T cells (Tregs). Mice blocked at different stages of T-cell development reveal that $CD4^+$ single-positive (SP) and CD8SP thymocytes differentially support homeostasis and activation of cDC1s versus cDC2s/ plasmacytoid DCs (pDCs), respectively. CD8SP regulate cDCs via interferon signaling, while CD4SP promote NF-kB activation. CD40, which activates non-canonical NF-kB signaling, is required for both activation and homeostasis of cDC1s, although only activation is driven by cognate interactions with CD4SPs. Surprisingly, some DCs display an activated signature in the absence of mature thymocytes. Altogether, this study comprehensively identifies functionally distinct thymic DC subsets and elucidates requirements for crosstalk with thymocyte subsets that support their homeostasis and activation.

INTRODUCTION

Thymic central tolerance protects against autoimmunity by enforcing selection of a self-tolerant T-cell repertoire. If developing T cells express T-cell receptors (TCRs) that bind with high affinity to self-antigens displayed by thymic antigen presenting cells (APCs), including medullary thymic epithelial cells (mTECs) and dendritic cells (DCs), they undergo negative selection or are diverted to the regulatory T cell (Treg) lineage, establishing central tolerance[1]. Thymic DCs play a crucial role in central tolerance, as genetic ablation of DCs results in impaired negative selection and ensuing autoimmunity[2]. In addition to displaying self-peptides from their own proteome, DCs acquire and present diverse self-antigens to establish self-tolerance, including tissue-restricted antigens (TRAs) expressed by *Aire*$^{+}$ mTECs, circulating antigens, and peripherally-acquired antigens[3].

The thymic DC compartment can be divided into three major subsets: conventional DC1s (cDC1s), cDC2s, and plasmacytoid DCs (pDCs)[4,5]. Thymic cDC1s and cDC2s can be further subdivided into non-activated CCR7^{-} MHC-II^{lo} and activated CCR7^{+} MHC-II^{hi} subsets[6–10]. Recent studies reveal additional heterogeneity within thymic cDC2s, underscoring the need for comprehensive assessment of thymic cDC composition and function[10–13]. Notably, cDC1s and cDC2s become activated in the sterile thymus environment, but our understanding of microenvironmental cues that support their homeostasis and activation remains limited. While cDC1s differentiate from progenitors intrathymically, cDC2s and pDCs are recruited to the thymus in a chemokine-dependent manner[11,12,14–16]. Within the thymus, CCR7 impacts cDC homeostasis by supporting survival of activated cDC1s (aDC1s), such that the frequency of cDC subsets is altered in *Ccr7*$^{-/-}$ mice[6]. Recently, type 2 cytokines have been implicated in supporting cDC2 homeostasis[10]. Activation of DCs in the thymus mirrors DC activation in the periphery,

resulting in upregulation of MHC and co-stimulatory molecules that enhance self-antigen presentation to thymocytes[4,7,8]. While pattern recognition receptor signaling seems to be dispensable for thymic DC activation, cognate interactions with CD4SP thymocytes have been reported to support cDC1 and cDC2 activation, in part via CD40 signaling[8,17]. Multiple signals are required to fully activate and license DCs in the periphery, raising the question of whether additional cues regulate the activation of thymic DC subsets.

Here, we employ single-cell RNA sequencing (scRNA-seq) and functional assays to identify transcriptionally distinct DC subsets in the mouse thymus, compare their APC activity, and discriminate cellular and molecular mediators of DC homeostasis and activation. Functional studies reveal that aDC1s most efficiently present mTEC-derived antigens, followed closely by aDC2s. In contrast, cDC2s and aDC2s most efficiently drive Treg selection. We find that CD4SPs and CD8SPs are required for homeostasis and activation of cDC1s and cDC2s, respectively, with CD8SPs also supporting pDC homeostasis. Additional analyses indicate that CD4SPs support cDC1 homeostasis and activation through CD40 signaling. In contrast, CD8SPs activate cDCs via interferon signaling. Unexpectedly, transcriptionally activated thymic DCs are present in the absence of mature thymocytes. Altogether, our study demonstrates substantial phenotypic and functional heterogeneity in the thymic DC compartment and identifies differential thymocyte signals that support homeostasis and activation of DC subsets.

RESULTS

scRNA-seq reveals significant transcriptional heterogeneity in thymic cDCs, which localize to distinct anatomical regions of the thymus

To comprehensively identify transcriptionally distinct thymic DC subsets, we performed scRNA-seq analysis of 8404 FACS-sorted $CD45^{+}MHC\text{-}II^{+}$ thymic

hematopoietic APCs (HAPCs) from 1 month-old C57BL/6J mice (Extended Data Fig. 1a,b). After dimensionality reduction and unsupervised clustering, we identified distinct HAPC subsets and thymocytes based on expression of lineage-specific genes (Extended Data Fig. 1b,c). cDCs were re-clustered and analyzed separately, enabling identification of 11 transcriptionally distinct cDC subsets: 5 *Xcr1*-expressing cDC1 clusters, 3 *Sirpa*-expressing cDC2 clusters, and 2 activated *Ccr7*-expressing "aDC" clusters that could be distinguished based on expression of cDC1 versus cDC2 markers (Fig. 1a,b and Extended Data Fig. 1d). In addition, we identified a heterogeneous "Ly6d^{+} cDC" cluster, which transcriptionally resembles pDCs, but can be distinguished by *Zbtb46* expression (Fig. 1b and Extended Data Fig. 1d,e). Ly6d^{+} cDCs share transcriptional similarity with cDC1s and cDC2s, as indicated by *Xcr1* and *Sirpa* expression (Fig. 1b).

cDC1 clusters express canonical cDC1 lineage-specific genes, including *Xcr1, Irf8, Cd36,* and *Cd24a* (Fig. 1b and Extended Data Fig. 1d)[10,18,19]. "CD207^{hi} Nur77^{-} cDC1s" express high levels of *Cd207* and *Itgae* (Fig. 1b and Extended Data Fig. 1d). Three "cycling cDC1" clusters express genes associated with cell proliferation (Fig. 1c and Extended Data Fig. 1d). "CD207^{lo} Nur77^{+} cDC1s" express high levels of *Nr4a1* (Nur77) and AP-1 family genes[20], including *Jun*, *Fos*, *Fosb*, and *Atf3* (Fig. 1b and Extended Data Fig. 1d).

cDC2 clusters express canonical cDC2-associated genes, including *Sirpa*, *Irf4*, *Mgl2*, and *Cd209a*[10,18] (Fig. 1b and Extended Data Fig. 1d). In addition to a "cycling cDC2" cluster, we identified an "EpCAM^{+} cDC2" subset, with high expression of *Epcam*, *Ltb*, and *Ccl17;* and a recently described[11–13] "MonoDC2" subset, expressing monocyte-associated markers such as *Cx3cr1*, *Cd14*, and *Ly6c2* (Fig. 1b and Extended Data Fig. 1d).

Activated "aDC" subsets, were identified by high expression of genes associated with DC maturation, such as *Ccr7*, *Cd63*, *Ccl5*, and *Ccl22* (Fig. 1b and Extended Data Fig. 1d)[7,8]. "aDC1" and "aDC2" subsets express the cDC1- and cDC2-lineage specific

transcription factors *Irf8* and *Irf4*, respectively (Fig. 1b) and correlate with CCR7$^+$ mature "mDC1" and "mDC2" clusters[10] (Extended Data Fig. 1f). Despite a strong shared DC activation gene signature (Extended Data Fig. 1d), differentially expressed genes discriminate aDC1s (e.g., *Il12b*) versus aDC2s (e.g., *Fabp5*) (Fig. 1b).

We established a flow cytometry panel to discriminate between cDC subsets identified by scRNA-seq (Extended Data Fig. 2a). CD207$^+$ cDC1s and Ly6d$^+$ cDC1s were within the XCR1$^+$ cDC1 compartment (Fig. 1d), with the remaining CD207$^-$ Ly6d$^-$ cDC1s (rcDC1) containing cycling and Nur77$^+$ cDC1 subsets (Fig. 1d). CD14$^+$ and/or CX3CR1$^+$ MonoDC2s were identified within the SIRPα$^+$ cDC2 compartment, with cycling and EpCAM$^+$ cDC2 clusters contained in the remaining CD14$^-$ CX3CR1$^-$ cDC2s (rcDC2) (Fig. 1d). High expression of CCR7 and CD63 identify aDCs , with XCR1 and SIRPα expression demarcating aDC1 and aDC2, respectively (Fig. 1d).

To validate that the 7 cDC subsets identified by flow cytometry correlate with their transcriptional counterparts, cDC subsets were FACS-isolated, hashtagged, and pooled prior to scRNA-seq analysis. UMAP-based dimensionality reduction revealed 6744 hashtagged cDCs distributed among 10 transcriptionally distinct clusters (Extended Data Fig 2b,c). Six of the FACS-isolated cDC subsets mapped to the expected cDC transcriptional cluster(s) (Extended Data Fig. 2d,e); insufficient numbers of Ly6d$^+$ cDC1s prevented accurate annotation of this subset. Notably, sorted CCR7$^+$ CD63$^+$ aDC1s and aDC2s mapped almost exclusively to the expected aDC clusters, confirming CCR7 and CD63 as markers of aDCs and of XCR1 and SIRPα in discriminating aDC subsets (Extended Data Fig. 2e).

Because thymocytes migrate between distinct microenvironments, where local APCs impact their differentiation and selection[21], we assessed the localization of thymic DC subsets (Fig. 1e and Extended Data Fig. 2f,g). All cDC and aDC subsets are present at

the highest densities in the medulla, where they can acquire and present mTEC-derived antigens to thymocytes (Fig. 1e and Extended Data Fig. 2g,h). Most cDC/aDC subsets are also present at the cortico-medullary junction (CMJ), although CD14^{+} MonoDC2s are located almost exclusively in central medullary regions. While some aDC2s appeared to localize to the cortex, most (83.1 %) of these cells were macrophages co-expressing Mertk (Extended Data Fig. 2f), consistent with reported cortical localization of thymic macrophages[22]. Thus, calculated densities of aDC2s were corrected to exclude macrophages (Extended Data Fig. 2h). Compared with other cDC/aDC subsets, CD207^{+} cDC1s are present at the highest density in the cortex, where they may promote central tolerance of early post-positive selection cortical thymocytes[23–25] (Extended Data Fig. 2i). Notably, pDCs are more abundant in the cortex than the other DC subsets (Fig. 1e and Extended Data Fig. 2g-i), in contrast to a prior report indicating medullary localization[14]. Altogether, thymic DC subsets are located in distinct anatomical niches, where they could interact with co-localized thymocyte subsets to establish robust central tolerance.

cDC subsets have distinct capacities to present mTEC-derived antigens and induce Treg differentiation

We next assayed thymic DC subsets for distinct functional activities. To test for cross-presentation of mTEC-derived TRAs on MHC-I, we co-cultured OT-I CD8^{+} T cells with thymic DC subsets FACS-sorted from RIP-mOVA and RIP-OVA^{hi} transgenic mice (Kurts et al., 1996; Kurts et al., 1998), in which mTECs express ovalbumin (OVA) as a model TRA. Regardless of whether OVA was expressed by mTECs in a membrane-bound (RIP-mOVA) or secreted (RIP-OVA^{hi}) form, aDC1s most efficiently cross-presented the TRA on MHC-I, inducing proliferation of the highest frequency and number of OT-I CD8^{+}

T-cells, which underwent more rounds of cell division (Fig. 2a-c and Extended Data Fig. 3a-c). Notably, although inferior to aDC1s (p-value <0.0001), aDC2s cross-presented OVA to stimulate more OT-I proliferation than non-activated cDC1 and cDC2 subsets (Fig. 2a-c and Extended Data Fig. 3a-c). Together, these data indicate that aDC1s are specialized for efficient cross-presentation of mTEC-derived antigens on MHC-I, with aDC2s contributing to this process.

Next, we compared the ability of cDC subsets to present mTEC-derived antigens on MHC-II. C57BL/6J bone marrow-derived hematopoietic progenitors were transplanted into lethally irradiated BALB/c recipient mice, yielding chimeric thymuses in which only radio-resistant BALB/c cells express I-Eα, while only hematopoietic cells, including cDCs, express I-A^b. Thus, cDCs must acquire I-Eα from mTECs for presentation on I-A^b, and the Eα:I-A^b complex can be detected by the Y-Ae antibody[7,28]. A high proportion of both aDC1s and aDC2s, followed by a lower frequency of rcDC2s and MonoDC2s acquired and presented mTEC-derived Eα on MHC-II (Fig. 2d). aDC1s presented the highest levels of Eα:I-A^b complexes, followed by aDC2s and then rcDC2s and MonoDC2s (Fig. 2e). These findings indicate that aDC1s followed closely by aDC2s efficiently present mTEC-derived antigens on MHC-II, with some presentation by remaining cDC2 subsets.

We next tested the capacity of different DC subsets to induce Treg generation. cDC subsets were FACS-sorted from C57BL/6J thymi and co-cultured with sorted $CD73^-CD25^-$ $Foxp3^-$ newly generated CD4SP thymocytes[29,30]. Interestingly, although aDC1s present the highest levels of mTEC-derived antigens on MHC-II (Fig. 2e), rcDC2s, MonoDC2s, and aDC2s were significantly more efficient at inducing Tregs relative to other DC subsets (Fig. 2f). Furthermore, within the heterogenous MonoDC2 population, $CD14^+$ MonoDC2s generated more Tregs than the $CD14^-$ MonoDC2s (Fig. 2g).

We considered whether differential expression of genes associated with MHC processing and presentation might underlie some of the functional differences between cDC subsets. Genes associated with MHC-I antigen processing and presentation, including *Psme1, Tapbp, Tap1,* and *Tap2* are most highly expressed by aDC1s, likely contributing to their superior ability to present antigens on MHC-I (Extended Data Fig. 3d). Compared to aDC1s, aDC2s express higher levels of genes associated with MHC-II antigen processing and presentation, such as *Cd74, Ciita, Ctsh, H2-Oa,* and *H2-DMa,* indicating that unlike aDC1s, aDC2s may continue to express new MHC-II molecules, possibly increasing the diversity of antigens presented (Extended Data Fig. 3d). *Cd83,* which stabilizes MHC-II at the cell surface, is upregulated by thymic aDCs, while *March1*, which increases degradation of MHC-II complexes, is downregulated (Extended Data Fig. 3d). Thus, consistent with DC activation in the periphery[31], thymic aDC1s and aDC2s express elevated cell-surface levels of MHC-II, as well as MHC-I (Extended Data Fig. 3e). Additionally, aDCs express higher levels of the costimulatory molecules CD80 and CD86 (Extended Data Fig. 3f,g), which are indispensable for thymocyte negative selection and Treg induction[32]. Because cDC2 subsets and aDC2s induce Tregs with similar efficiencies, but express different levels of MHC-II and co-stimulatory molecules, other factors must account for the preferential ability of the cDC2-lineage to induce Tregs (Fig. 2f and Extended Data Fig. 3e,g).

Thymic cDC1 and cDC2 homeostasis and activation depend on the presence of distinct thymocyte subsets

While it is established that cDC1s differentiate from progenitors intrathymically, and cDC2s migrate to the thymus from the periphery[4,5], the cellular and molecular cues required for homeostasis and activation of DC subsets within the thymus remain

unresolved. Presentation of self-antigens to CD4SP thymocytes has been implicated in activation of both cDC1 and cDC2 subsets[8]. Given the significant heterogeneity of thymic DCs revealed by scRNA-seq analyses, we sought to determine if different thymocyte cues regulate homeostasis and activation of distinct cDC subsets.

We first analyzed the thymic cDC compartment in *Rag2*$^{-/-}$ mice, in which thymocyte differentiation is blocked past the CD4^{-}CD8^{-}CD25^{+}CD44^{-} double-negative 3 (DN3) stage[33], and in *Tcra*$^{-/-}$ mice, in which thymocytes cannot pass positive selection and are blocked past the CD4^{+}CD8^{+} double-positive (DP) stage[34]. In both *Rag2*$^{-/-}$ and *Tcra*$^{-/-}$ mice, the cellularity of all cDC subsets and pDCs declined (Fig. 3a,b) with a substantial drop in numbers and frequencies of Ly6d^{+} cDC1s and aDCs (Fig. 3a,b and Extended Data Fig.4a,b). Thus, post-positive selection thymocytes are required for homeostasis of pDCs and cDCs and for cDC activation. Notably, the proportional representation of aDC1 and aDC2 remained unchanged in *Rag2*$^{-/-}$ and *Tcra*$^{-/-}$ mice relative to wild-type (WT) controls, indicating that post-positive selection thymocytes are required for activation of both cDC1s and cDC2s (Extended Data Fig.4a,b).

B2m$^{-/-}$ mice were analyzed next to evaluate the contribution of CD8SP thymocytes to pDC and cDC homeostasis and activation. β2m-deficiency resulted in fewer pDCs and MonoDC2s (Fig. 3c and Extended Data Fig. 4c), highlighting a role for CD8SP thymocytes in pDC and cDC2 homeostasis. Interestingly, the number of aDC2s, but not aDC1s, declined significantly in *B2m*$^{-/-}$ mice (Fig. 3c). Since *B2m*$^{-/-}$ mice lack invariant natural killer T cells (iNKT), as well as CD8SP thymocytes, we tested if iNKT deficiency could account for altered DCs in *B2m*$^{-/-}$ mice but found no deviation in thymic DC numbers or proportions in *Cd1d*$^{-/-}$ mice (Extended Data Fig. 4d). Together, these results indicate that CD8SP thymocytes support homeostasis of pDCs and MonoDC2s and activation of cDC2s.

Thymic DCs in *MHC-II*$^{-/-}$ mice were analyzed to test the contribution of CD4SP cells to DC homeostasis and activation. pDC numbers remained unaltered in the absence of CD4SPs, confirming a non-redundant role for CD8SPs in regulating pDC homeostasis (Fig. 3d). CD207^{+} cDC1s and rcDC1s declined significantly in the absence of CD4SP thymocytes, as did rcDC2s (Fig. 3d and Extended Data Fig. 4e). Based on previous findings[8], we anticipated that CD4SP deficiency would result in fewer aDC1s and aDC2s; however, while the number and proportion of aDC1s was significantly reduced, aDC2s were surprisingly intact (Fig. 3d and Extended Data Fig. 4e). Of note, the decline in aDC subsets was more pronounced in *Rag2*$^{-/-}$ and *Tcra*$^{-/-}$ mice than in mice deficient for either individual SP subset (Fig. 3a-d), indicating some redundancy in the ability of CD4SP and CD8SP thymocytes to support thymic DC activation.

Altogether, our findings show that CD4SP thymocytes primarily regulate cDC1 homeostasis and activation while CD8SP thymocytes regulate pDC and MonoDC2 homeostasis, as well as cDC2 activation.

scRNA-seq profiling identifies the presence of unique DC transcriptional states in the absence of thymocyte crosstalk

To identify candidate mechanisms underlying the ability of different thymocyte subsets to support thymic DC homeostasis and activation, we performed scRNA-seq on HAPCs from *MHC-II*$^{-/-}$, *B2m*$^{-/-}$ and *Rag2*$^{-/-}$ thymi (Extended data Fig. 5a,b). Upon re-clustering cDCs separately, we identified 17 transcriptionally unique cDC subsets distributed across the 4 genotypes: 7 cDC1, 6 cDC2, 1 Ly6d^{+} cDC, and 3 aDC subsets (Fig. 4a-b and Extended Data Fig. 5c), indicating enhanced heterogeneity beyond that

observed in WT cDCs alone (Fig. 1a). We validated that genotype-specific cDCs were derived from the anticipated knockout (KO) mice (Extended Data Fig. 5d,e).

Five cDC1 clusters were similar to those identified in WT mice alone (Fig. 1a): CD207^{hi} Nur77^{-} cDC1, 3 cycling cDC1 subsets, and CD207^{lo} Nur77^{+} cDC1 (Fig. 4b,c). Two additional cDC1 clusters were primarily detected in KO genotypes (Fig. 4d-e): "CD207^{lo} Nur77^{-} cDC1" which are transcriptionally similar to CD207^{lo} Nur77^{+} cDC1s, except for lack of expression of genes including *Nr4a1* (Nur77), *Il1b*, *Fos*, and *Atf3*, and "Traf1^{+} cDC1s", which express elevated *Traf1*, a critical molecule in NF-kB signaling[35] (Fig. 4b and Extended Data Fig. 5c). Consistent with our flow cytometry data (Extended Data Fig. 4e), the frequency of cDC1s declines in CD4SP-deficient *MHC-II*$^{-/-}$ scRNA-seq datasets (Extended Data Fig. 5f). Notably, the frequency of CD207^{hi} Nur77^{-} cDC1s decreases in datasets from *B2m*$^{-/-}$ and *Rag2*$^{-/-}$ mice, counterbalanced by expansion of CD207^{lo} Nur77^{-}, CD207^{lo} Nur77^{+}, and Traf1^{+} cDC1s (Fig. 4d,e). Thus, the absence of CD8SP cells alters the transcriptional states of cDC1s, indicating a role for CD8SPs in cDC1 homeostasis beyond what was detectable by flow cytometry (Fig. 3c and Extended Data Fig. 4c).

Three of the cDC2 clusters were previously detected in WT cDC datasets (Fig. 1a): EpCAM^{+} cDC2, cycling cDC2, and MonoDC2 (Fig. 4b,c). Two cDC2 clusters emerged that were largely derived from *Rag2*$^{-/-}$ thymi (Fig. 4d,f): "Clec4^{+} cDC2", with high expression of *Lyz2* and C-type lectin receptors such as *Clec4a2*, and "Nur77^{+} cDC2", with a partially overlapping transcriptional signature with Nur77^{+} cDC1s (Fig. 4b and Extended Data Fig. 5c). We also identified a transitional cDC2 ("TrDC2") subset, likely in the process of activation, as it expresses genes characteristic of non-activated cDC2s (e.g., *Ltb* and *Sirpa*) and low levels of activation-associated genes (e.g *Ccr7* and *Cd63*) (Fig. 4b and Extended Data Fig. 5c). Consistent with CD8SP support of cDC2 homeostasis (Fig. 3c and

Extended Data Fig. 4c), cDC2 frequencies decline in *B2m*$^{-/-}$ scRNA-seq datasets (Extended Data Fig. 5f), and the proportion of MonoDC2s within cDC2 clusters declines in *B2m*$^{-/-}$ and *Rag2*$^{-/-}$ mice (Fig. 4f). The frequency of EpCAM^{+} cDC2s declines substantially in the *Rag2*$^{-/-}$ thymus, counterbalanced by expansion of Clec4^{+} cDC2s (Fig. 4f), reflecting a larger transcriptional shift in cDC2s in the absence of SP thymocytes than revealed by flow cytometry.

We detected aDC1 and aDC2 clusters, as well as a novel aDC cluster with high expression of *Il15ra* ("Il15ra^{hi} aDC") and lower expression of *Ccr7* and *Cd63* that was primarily derived from the three KO strains (Fig. 4b,d,g). Surprisingly, though flow cytometry showed that aDCs were greatly diminished in *Rag2*$^{-/-}$ thymi (Fig. 3a), scRNA-seq revealed the presence of a substantial pool of aDCs in *Rag2*$^{-/-}$ thymuses (Fig. 4d and Extended Data Fig. 5f) suggesting molecular cues independent of DP and SP thymocytes can contribute to cDC activation.

In summary, scRNA-seq data of thymic DCs from *B2m*$^{-/-,}$ *MHC-II*$^{-/-,}$ and *Rag2*$^{-/-}$ mice corroborate that different thymocyte subsets directly or indirectly support homeostasis and activation of distinct DC subsets and reveal additional transcriptional changes in cDCs in the absence of thymocyte subsets beyond those apparent by flow cytometry.

CD4SP and CD8SP thymocytes promote DC homeostasis and activation via distinct pathways

To determine how CD4SP and/or CD8SP thymocytes alter transcriptional programs associated with cDC activation, we inferred the differentiation trajectories of WT cDC1s and cDC2s using p-Creode, an unsupervised algorithm for single-cell trajectory

inference[36]. RNA velocity analysis confirmed the directionality of differentiation from cDC1s to aDC1s and cDC2s to aDC2s, respectively (Extended Data Fig. 6a). One end of each p-Creode trajectory represents progenitor-like cDCs with a high degree of transcriptional diversity as indicated by the high CytoTRACE scores[37], while the other end represents activated cDCs with restricted differentiation potential, indicated by low CytoTRACE scores (Extended Data Fig. 6b). To determine the identity of each transcriptional state along the p-Creode trajectories, we assessed the proportion of UMAP-based cDC clusters (Fig. 4a) comprising each node, which revealed that differentiation proceeds from proliferating to activated cDC subsets in each WT trajectory (Fig. 5a,b).

To determine how deficiencies in thymocyte subsets alter cDC differentiation, scRNA-seq data from KO DCs were projected onto WT p-Creode trajectories. Compared to WT cDC1 and cDC2 trajectories, some differentiation nodes were not populated by cells along the transition to activated DC states in *MHC-II*$^{-/-}$, *B2m*$^{-/-}$, and *Rag2*$^{-/-}$ mice, indicating dysregulated cDC differentiation in the absence of SP thymocyte subsets (Fig. 5a,b). Dysregulated differentiation is further indicated by the altered subset composition of nodes along each trajectory in the KO strains, such as the appearance of CD207^{lo} Nur77^{-} and CD207^{lo} Nur77^{+} cDC1 cells within nodes approaching the location of aDC1s in *Rag2*$^{-/-}$ mice or the prevalence of Nur77^{+} cDC2 cells among cDC2 progenitors in *B2m*$^{-/-}$ and *Rag2*$^{-/-}$ mice (Fig. 5a,b).

The unexpected presence of aDC1s and aDC2s in *Rag2*$^{-/-}$ scRNA-seq datasets indicates that cDCs undergo at least partial activation without crosstalk from SP thymocytes (Fig. 4d). Relative to aDCs from WT mice, *Rag2*$^{-/-}$ aDCs express lower levels of genes associated with full cDC activation, including *Ccr7, Cd63, H2-Ab1, Cd80, Cd86,* and *Cd40* (Extended Data Fig. 6c,d), suggesting they may require “licensing” signals from thymocytes to fully upregulate MHC and costimulatory molecules[38]. Lower expression of

these genes could explain why CCR7^{+} CD63^{+} aDCs are not detected by flow cytometry in *Rag2*$^{-/-}$ mice despite the significant aDC population identified by scRNA-seq. The replacement of WT-like aDC nodes by Il15ra^{hi} aDCs (Fig. 5a) in all KO strains also suggests alternate cDC activation signals in the absence of SP thymocyte-derived cues.

To elucidate mechanisms by which SP thymocytes support thymic DC activation, genes differentially expressed along the trajectory of cDC1 or cDC2 differentiation were identified between WT and KO genotypes using tradeSeq analysis[39] and then evaluated via pathway enrichment analysis (Fig. 5c,d). In *MHC-II*$^{-/-}$ mice, CD4SP deficiency resulted in upregulation of genes associated with Interferon alpha (Type I) and Interferon gamma (Type II) signaling along the trajectory of cDC1 and cDC2 activation; conversely, expression of genes associated with IFNα and IFNγ signaling was reduced along cDC1 and cDC2 trajectories in *B2m*$^{-/-}$ and *Rag2*$^{-/-}$ mice (Fig. 5c,d and Extended Data Fig. 7a,b). Together, these results suggest that CD8SP thymocytes promote interferon signaling in differentiating thymic cDCs. In *MHC-II*$^{-/-}$ mice, genes associated with CD40 signaling were expressed at lower levels along the cDC1 trajectory, indicating CD4SP thymocytes support cDC1 homeostasis and activation through CD40-dependent non-canonical NF-kB signaling (Fig. 5c). Interestingly, genes associated with antigen processing and presentation machinery decline in cDC1s in the absence of CD4SPs or CD8SPs, but decline in cDC2s more considerably in the absence of CD8SPs, highlighting the role of CD8SPs in cDC2 activation (Fig. 5c,d).

The absence of both CD4SP and CD8SP thymocytes in *Rag2*$^{-/-}$ mice results in increased canonical NF-kB signaling and IL-6-JAK/STAT3 signaling, along with a stark decline in IL-12 signaling in aDC1s and aDC2s, further indicating an altered transcriptional state is associated with the aDCs that persist without crosstalk from SP thymocytes (Fig. 5c,d and Extended Data Fig. 7c). Altogether, analysis of differentially regulated gene

expression along the trajectory of cDC1 and cDC2 activation indicates that interferon signaling, which requires CD8SP cells, and NF-kB signaling, which requires CD4SP cells, cooperate to support cDC homeostasis and activation in the thymus.

Cognate interactions with CD4SP thymocytes and CD40-CD40L interactions are differentially required for cDC1 homeostasis versus activation

We next investigated mechanisms by which CD4SP thymocytes promote cDC1 homeostasis and activation. Cognate interactions between CD4SP thymocytes and cDCs are reported to promote thymic cDC activation via CD40 signaling[8,17], and CD40L is predominantly expressed by CD4SP thymocytes[40]. Our analyses revealed that CD40 signaling declines in differentiating cDC1s in the absence of CD4SP cells (Fig. 5d). Furthermore, genes involved in or targets of non-canonical NF-κB signaling, including *Nfkb2*, *Icam1*, *Relb*, *Bcl2a1b*, and *Traf2*[41,42], were downregulated in *MHC-II*$^{-/-}$ cDC1s and aDC1s (Fig. 6a). Thus, we tested whether CD40 signaling and cognate interactions with CD4SP thymocytes regulate cDC1 homeostasis and/or activation.

We analyzed thymic cDCs in *Xcr1*$^{cre/+}$ *Cd40*$^{f/-}$ mice, in which CD40 deficiency is restricted to the cDC1/aDC1 compartment (Extended Data Fig. 7d)[43]. Transcriptional and flow cytometry analyses show that CD40 is more highly expressed by aDC1s relative to non-activated cDC1 subsets (Fig. 6b,c), suggesting CD40 deficiency might impact only cDC1 activation. However, cDC1-specific CD40 deficiency diminished the cellularity of all cDC1 subsets, with an almost complete ablation of CD207^{+} cDC1s and aDC1s (Fig. 6d). As expected, cDC1-specific CD40 deficiency did not alter cDC2 or aDC2 cellularity (Fig. 6d). Thus, CD40 signaling is essential for thymic cDC1 homeostasis and activation.

To test if impaired cDC1 homeostasis and activation in *MHC-II*$^{-/-}$ mice reflected the absence of cognate interactions between CD4SP thymocytes and cDC1s, we analyzed thymic cDCs from *Itgax*$^{cre/+}$ *I-Ab*$^{f/f}$ mice, in which CD4SP thymocytes are present, and only DCs lack MHC-II expression (Extended Data Fig. 7e). Notably, cognate interactions with CD4SP thymocytes were not required for cDC1 homeostasis (Fig. 6e), despite the requirement for CD40 (Fig. 6d). Thus, cell types in addition to CD4SP cells may provide CD40L to support cDC1 homeostasis, or CD4SPs may provide CD40L through non-cognate interactions. Reduced cellularity of aDC1s in *Itgax*$^{cre/+}$ *I-Ab*$^{f/f}$ mice is consistent with a requirement for antigen presentation on MHC-II to CD4SPs for cDC1 activation (Fig. 6e)[8]. However, this reduction in aDC1 cellularity is less extreme than in *Xcr1*$^{cre/+}$ *Cd40*$^{f/-}$ mice, reflecting either the paucity of non-activated cDC1s that could become activated in *Xcr1*$^{cre/+}$ *Cd40*$^{f/-}$ mice (Fig. 6d), activation of CD40 signaling in cDC1s by cells other than CD4SPs in *Itgax*$^{cre/+}$ *I-Ab*$^{f/f}$ mice, or activation of CD40 signaling via non-cognate interactions with CD4SPs. Analysis of the cDC2 compartment in *Itgax*$^{cre/+}$ *I-Ab*$^{f/f}$ mice showed that rcDC2s and MonoDC2s do not require antigen presentation on MHC-II to CD4SP cells for their maintenance (Fig. 6e), though rcDC2s declined significantly in *MHC-II*$^{-/-}$ thymi (Fig. 3d), suggesting non-cognate interactions with CD4SP may promote rcDC2 homeostasis. Consistent with findings from *MHC-II*$^{-/-}$ mice, only activation of cDC1s, not cDC2s, was impaired when DCs could not present antigens to CD4SP thymocytes (Fig. 6e).

Altogether, these findings indicate that cognate interactions with CD4SP thymocytes are important for activation, but not homeostasis of cDC1s, while CD40-CD40L signaling is critical for both cDC1 homeostasis and activation.

DISCUSSION

Though recent studies have documented roles for several DC subsets in thymocyte selection[3], the relative ability of DC subsets to present TRAs on MHC-I and MHC-II and their capacity to induce Treg differentiation have not been comprehensively compared; furthermore, the cellular and molecular crosstalk signals that support homeostasis and/or activation of thymic DC subsets remain largely enigmatic. Here, we first identify the transcriptionally distinct subsets that comprise the thymic DC compartment through scRNA-seq at greater resolution than previously described[10,22,44]. We then elucidate the distinct functional abilities of these DC subsets, as well as the microenvironmental signals that support their homeostasis and activation.

Our functional studies reveal that while both activated DC subsets express high levels of MHC and co-stimulatory molecules and can acquire mTEC-derived antigens, the DC1 and DC2 lineages differ in the efficiency with which they induce T cell proliferation versus Treg differentiation. aDC1s are the most efficient at acquiring and presenting mTEC-derived antigens on MHC-I and MHC-II, followed by aDC2s. *Cd36*, a scavenger receptor that facilitates acquisition of cell-surface proteins from apoptotic mTECs[45], is expressed exclusively by cDC1 subsets (Fig. 1b), indicating that cDC2s must use alternative mechanisms to acquire mTEC-derived antigens, possibly via trogocytosis, exosome transfer, or gap junctions[3]. All cDC2 subsets and aDC2 efficiently induced CD4SP Treg differentiation, in agreement with reports from our lab and others that cDC2s more efficiently induce Tregs in vitro than cDC1s or pDCs[6,30,46]. However, aDC1s have been reported to select some TRA-specific Tregs[45,47], which may reflect increased presentation of mTEC-derived antigens on MHC-II by this subset. Mechanisms by which cDC2/aDC2 more efficiently induce Tregs relative to cDC1/aDC1 remain to be determined.

Few microenvironmental signals that support DC homeostasis and activation within the thymus have been elucidated. Cognate interactions with CD4SP thymocytes CD40 signaling were previously reported to be required for activation of thymic cDC1s and cDC2, while a role for CD8SPs was not identified[8,17]. In contrast, our data reveal that CD4SP and CD8SP thymocytes play distinct, essential roles in regulating homeostasis and activation of cDC1s versus cDC2s, respectively. Such divergent conclusions may reflect the refined gating schemes we used to identify aDCs, informed by scRNAseq analyses. pDCs enter the thymus from circulation[4] and can induce central tolerance to peripherally-acquired antigens[14,15]. Unexpectedly, β2m deficiency resulted in a substantial reduction in pDC cellularity, implicating CD8SPs in regulating pDC recruitment and/or homeostasis, with underlying mechanisms remaining to be resolved.

Additional scRNA-seq analyses of thymic cDCs from *B2m*$^{-/-}$, *MHC-II*$^{-/-}$ and *Rag2*$^{-/-}$ mice suggest that CD4SPs promote cDC1 differentiation and activation through CD40-dependent non-canonical NF-kB signaling, while CD8SPs induce interferon signaling to regulate cDC2 homeostasis and activation. Additionally, CD8SP deficiency also resulted in reduced interferon signaling in cDC1s. In the context of infections, interferon signaling promotes peripheral DC activation and enhanced expression of costimulatory molecules for effective naïve T cell stimulation[48,49]. In the thymus, even without infectious stimuli, mTECs express Type I IFN (IFNβ) and Type III IFN (IFNλ), which could modulate DC activation[50,51]. Hence, SP thymocytes could directly signal to DCs to promote their differentiation, or they could impact other cells in the thymus, such as TECs, with secondary consequences for cDC activation.

We tested the hypothesis, suggested by scRNA-seq analyses, that CD40 is required for cDC1 homeostasis and activation. We found that CD40 signaling not only drives cDC1 activation, as previously reported[8,17], but is also crucial for cDC1 homeostasis, as all cDC1

subsets declined significantly when cDC1s selectively lacked CD40 expression. However, antigen presentation on MHC-II is necessary for cDC1 activation, but not for cDC1 homeostasis. Thus, although CD4SP thymocytes are the major source of CD40L in the thymus[40], other cellular sources of CD40L, such as iNKTs which have been shown to induce IL-12 production in cDC1s through CD40-CD40L interactions[52], could support thymic cDC1 homeostasis. An alternative source of CD40L beyond CD4SPs could also account for the more significant decline in cDC1 subsets in cDC1-specific CD40-deficient mice versus *MHC-II*$^{-/-}$ mice. iNKT cells would play a redundant role in providing CD40L, as cDC subsets were intact in iNKT-deficient *Cd1d*$^{-/-}$ thymi. Another possibility is that CD4SP thymocytes may provide CD40L to cDC1 in a non-cognate manner[53].

Despite the lack of DP and SP thymocytes in *Rag2*$^{-/-}$ thymuses and failure to detect aDCs by flow cytometry, a significant population of aDCs were present in scRNA-seq data from *Rag2*$^{-/-}$ thymi. Interestingly, interferon-response genes and IL-12 signaling decline starkly in *Rag2*$^{-/-}$ aDC1s and aDC2s, while genes associated with canonical NF-kB signaling and IL-6-JAK/STAT3 pathways increase, suggesting alternative mechanisms of DC activation in the absence of SP thymocytes. IL-6/STAT3 signaling has been shown to suppress efficient DC activation[54], which could partially explain the lower levels of activation and costimulatory genes expressed by *Rag2*$^{-/-}$ aDCs. Additionally, it is possible that pre-β-selection DN thymocytes, which are intact in *Rag2*$^{-/-}$ thymi and express TNFSF ligands such as RANKL and TNF-α[40], could induce canonical NF-kB signaling in DCs. Finally, the reduction in IL-12 signaling could reflect the loss of iNKT cells in *Rag2*$^{-/-}$ mice[52].

Future studies will test whether the candidate molecular cues identified herein by which thymocytes alter DC homeostasis and activation directly regulate DC subsets or modulate other cells in the thymus environment, which subsequently impact thymic DCs.

Understanding mechanisms of thymocyte-DC crosstalk would provide a framework for altering the thymic DC activation state to efficiently promote selection of a self-tolerant T cell pool.

METHODS

Mice

C57BL/6J (Wild-type; WT; B6), BALB/cJ, B6.SJL-Ptprc^{a}PepC^{b} (CD45.1), C57BL/6-Tg(TcraTcrb)1100Mjb/J (OT-I), C57BL/6- Tg(Ins2- TFRC/OVA) 296Wehi/WehiJ (RIP- mOVA) [26], RIP- OVA^{hi} [27] (W. R. Heath, University of Melbourne, Melbourne, Australia), B6(Cg)-Rag2$^{tm1.1Cgn}$/J (*Rag2*$^{-/-}$), B6.129S2-H2$^{dlAb1-Ea}$/J (*MHCII*$^{-/-}$), B6.129P2-B2m^{tm1Unc}/DcrJ (*B2m*$^{-/-}$), B6.129S6-Del(3Cd1d2-Cd1d1)1Sbp/J (*Cd1d*$^{-/-}$), B6.129S2-Tcra^{tm1Mom}/J (*Tcra*$^{-/-}$), Foxp3$^{tm9(EGFP/cre/ERT2)Ayr}$/J, *Xcr1*$^{cre/+}$ *Cd40*$^{f/-}$ [43] (K. Murphy, Washington University School of Medicine, St. Louis, Missouri, USA), B6.Cg-Tg(Itgax-cre)1-1Reiz/J (CD11c-cre) and B6-129X1-*H2-Ab1*^{tm1Koni}/J strains were bred in-house. Experiments were performed using 6–8-week-old mice of both sexes. All strains were purchased from The Jackson Laboratory unless otherwise specified. Mice were maintained under specific pathogen-free conditions at the Animal Resources Center, the University of Texas at Austin. All experimental procedures were performed in accordance with the Institutional Animal Care and Use Committee.

Flow cytometry and FACS

For isolating thymic cDCs and TECs, thymi of the appropriate genotypes were isolated, cut into small pieces, and enzymatically digested as previously described [55].

Briefly, each thymus was digested in 2mL of enzymatic mixture containing Liberase™ (Roche) and DNAse I (Roche) in PBS at 37°C for 12 minutes, gently swirling the tubes mid-interval (6 minutes). After digestion, supernatant containing cells released from the tissue was transferred into 30mL of FACS-wash buffer (FWB)+ EDTA (PBS+ 2% bovine calf serum (BCS) + 5mM EDTA) and stored on ice. The enzymatic digestion step was repeated twice on residual tissue fragments to ensure complete dissociation of the tissue. Digested cells were centrifuged in 2mL of FWB+EDTA at 300g for 5 minutes at 4°C, the supernatant was discarded (henceforth referred to as "washing the cells"), and the cell pellet was resuspended in FWB+ EDTA. For thymic DC flow cytometry panels that included anti- CCR7, 6 x 10^6 cells were stained with the indicated cocktail of fluorophore conjugated-antibodies in 200µL FWB for 40 minutes at 37°C before washing the cells once and resuspending in FWB+EDTA with 0.1µg/mL propidium iodide (Enzo).

For thymocyte staining panels that included anti-FoxP3, thymocyte single cell suspensions were generated by pressing thymi through 40µm cell strainers, which were rinsed with FWB. 6 x 10^6 cells were stained with the appropriate cocktail of cell-surface conjugated antibodies in 200µL FWB with the fixable viability dye Zombie Red (BioLegend; 1:1000) for 30 minutes on ice. After washing the cells once in FWB and resuspending the pellet in 200µL of FWB (PBS + 2% BCS), cells were fixed and permeabilized with the Foxp3 Transcription factor staining Buffer kit according to manufacturer's recommendations (Tonbo Biosciences), followed by intracellular staining with anti-Foxp3-PE (ThermoFisher) for 30 minutes on ice. To FACS-sort CD4SP thymocytes, after antibody staining, cells were washed with FWB and resuspended in FWB plus propidium iodide (Enzo), as above. For functional assays, cells were FACS sorted into PBS+ 10% BCS.

For flow cytometry analysis or FACS-isolation of the indicated cell types, cocktails of the following fluorescent-conjugated antibodies were used- CD11b (M1/70), CD11c (N418), SIRPα (P84), CX3CR1 (SA011F11), XCR1 (ZET), F4/80 (BM8), Ly6d (49-H4), PDCA-1 (927), CD14 (M14-23), CD207 (4C7), CCR7 (4B12), CD63 (NVG-2),I-A/I-E (M5/114.15.2), CD19 (1D3), CD90.2 (53-2.1), CD45 (30-F11), Y-Ae (eBioY-Ae), Vα2 (B20.1), Vβ5 (MR9-4), TCRβ (H57-597), CD3 (145–2C11), CD45.1 (A20), CD80 (16-10A1), CD86 (A17199A), CD40 (FGK45), H2-Kb (AF6-88.5), CD4 (RM4-5), CD8 (53-6.7), CD25 (PC61), FOXP3 (FJK-16s), CD73 (TY/11.8), and EpCAM (G8.8). All antibodies were obtained from BioLegend, eBioscience or BD Biosciences. All antibodies were used at a 1:400 dilution to stain the respective cell types (6 x 10^6 cells in 200 µL volume) except as noted: CCR7-APC (1:200), I-A/I-E-APC/Cy7 (1:5000), FOXP3-PE (1:200), and EpCAM-PE (1:800).

Flow cytometry analysis was carried out on a BD LSRFortessa™ or a BD FACSAria™ Fusion. All FACS-sorting was carried out on a BD FACSAria™ Fusion. Flow cytometry data were analyzed using FlowJo software (V10.8.0, BD Biosciences).

FACS-isolation of cDC subsets for functional assays

Thymi from 5 mice of the appropriate genotypes were extracted for the corresponding assays, and enzymatically digested as described above to isolate thymic DCs. Prior to FACS-sorting DC subsets, a DC-enrichment step was carried out: after washing the cells in FWB+EDTA following enzymatic digestion, they were washed and stained with CD11c-Biotin (N418, Biolegend) for 20 minutes at 4°C. After washing once in FWB+EDTA, the cells were incubated with 10µL of Streptavidin Microbeads (Miltenyi Biotec) per 10^7 cells for 15 minutes on ice and then washed once with FWB+EDTA.

CD11c-stained cells were positively enriched using MACS LS columns in the magnetic field of a MidiMACS separator according to the manufacturer's protocol. CD11c-enriched cells were then stained with antibodies against CCR7, CD11b, CD11c, CD14, CD63, CD207, CX3CR1, F4/80, Ly6d, MHC-II, PDCA-1, SIRPα, and XCR1 for FACS-sorting the 8 DC subsets –pDCs (SSC-A^{lo} PDCA1^{+} CD11c^{+}), CD207^{+} cDC1s, Ly6d^{+} cDC1s, rcDC1s (Ly6d^{-} CD207^{-}), MonoDC2s (CD14^{+} and/or CX3CR1^{+}), rcDC2s (CD14^{-} CX3CR1^{-}), aDC1s (CCR7^{+} CD63^{+} XCR1^{+}), and aDC2s (CCR7^{+} CD63^{+} SIRPα^{+}) - using the gating strategy shown in Extended Data Fig. 2a.The 8 DC subsets were sorted into PBS+ 10% BCS using a 100um nozzle on the BD FACSAria^{TM} Fusion.

In vitro OT-I DC stimulation assays

Thymic DC subsets were FACS-sorted as described above from RIP-mOVA and RIP-OVA^{hi} mice and resuspended at a cell concentration of 10,000 cells/100µL in complete RPMI (RPMI 1640 (Gibco), 10% fetal bovine serum (FBS; Gemini Bio-Products), 1 mM Sodium Pyruvate (Gibco), 1x GlutaMAX (2 mM L-alanyl-L-glutamine dipeptide; Gibco), 1x MEM Non-essential Amino Acid Solution (Sigma-Aldrich), 1x Penicillin-Streptomycin-Glutamine (100 units of penicillin, 100 µg of streptomycin, and 292 µg/ml of L-glutamine; Gibco), and 55 µM β-mercaptoethanol (Gibco)). CD8^{+} T cells were enriched from the spleen of OT- I mice using the Mojosort^{TM} Mouse CD8^{+} T cell isolation kit (Biolegend) and stained with 5µM CellTrace Violet (Thermo Fisher) according to manufacturers' instructions. Enriched CellTrace Violet-labeled OT-I CD8^{+} T cells were resuspended at 20,000 cells/100uL in complete RPMI + 10ng/mL of recombinant mouse IL-2 (Biolegend). As positive control, WT splenocytes were pulsed with 50nM exogenous OVA$_{257-264}$ (SIINFEKL) peptide (New England Peptide) for 30 minutes at 37°C and then

washed once with complete RPMI following incubation. cDC subsets from the RIP-mOVA or RIP-OVA^{hi} mice or OVA$_{257-264}$ -pulsed WT splenocytes were cocultured with CellTrace Violet-labeled OT-I CD8^{+} T cells at a 1:2 ratio for 3.5 days at 37°C for before CD8^{+} T cell proliferation was assessed by flow cytometry. The number of cell divisions was determined using the proliferation modeling tool in FlowJo™ software. Unstimulated CD8^{+} T cells were used to identify "Generation 0" peak, and a peak ratio close to 0.5 percent was implemented, indicating that every cell division results in half as much dye in the cells from the next generation. Each proliferation peak was gated by the tool to determine the percentage and number of cells associated with distinct rounds of cell division.

In vitro Treg generation assays

Treg generation assays were set up as previously described [30]. 7 cDC subsets and 1 pDC subset were FACS-sorted as discussed above from 4-5 pooled B6 thymi and each subset was reconstituted at a concentration of 10,000 cells/100µL in complete RPMI. CD73^{-} CD4^{+} CD25^{-} Foxp3^{-} newly generated CD4SP thymocytes were sorted from *Foxp3*$^{eGFP\text{-}Cre\text{-}ERT2}$ reporter mice and reconstituted at a concentration of 20,000 cells/100uL in complete RPMI + 100ng/mL recombinant mouse IL-7 (Biolegend). CD4SP thymocytes and DC subsets were co-cultured at a 2:1 ratio in round-bottom 96-well plates for 4 days and then analyzed by flow cytometry on day 5 to evaluate the percentage of Tregs generated in vitro.

FACS purification of thymic HAPC and cDC subsets for scRNA-sequencing

To sort HAPCs for scRNA-sequencing, thymi were harvested and enzymatically digested as described above. After staining with a cocktail of antibodies, as shown in Extended Data Fig. 1a, cells were resuspended in FWB+EDTA plus propidium iodide (Enzo) for FACS-sorting. Sorted cells were washed into FWB without EDTA, counted and resuspended at a concentration of 700-1200 cells/µL prior to submission to The University of Texas at Austin's Genomic Sequencing and Analysis Facility (GSAF) core.

For hashtagging FACS-isolated cDC-subsets, $CD11c^+$ cells were enriched with MACS Streptavidin microbeads, as described above, and stained with the cell surface antibody sorting panel used to delineate cDC subsets, as indicated in Extended Data Fig. 2a. After the 7 cDC subsets were FACS-sorted, each was incubated with a distinct TotalseqB Hashtag antibody (Biolegend) at $0.05\mu g/10^6$ cells concentration for 30 minutes at 4°C. After staining with the Hashtag antibodies, the cells were washed four times in FWB before pooling 10,000 cells of each sorted DC population, with the exception of $Ly6d^+$ cDC1s for which there were fewer remaining cells than the other 6 populations at the end of the protocol. Cells were spun down in FWB without EDTA and resuspended at a concentration of 700-1200 cells/µL prior to sample submission for scRNA-sequencing to the GSAF core.

scRNA-seq library preparation

Single cell suspensions were processed for scRNA-seq at UT Austin GSAF. Cell suspensions were loaded on a Chromium Controller (10X Genomics) and processed for cDNA library generation following the manufacturer's instructions for the Chromium NextGEM Single Cell 3' Reagent Kit v3.1 (10X Genomics). For hashtagged FACS-sorted

DC samples, Cell surface protein libraries were constructed using the Chromium NextGEM Single Cell 3' Reagent Kit v3.1 with Feature Barcoding technology (10X Genomics). The resulting libraries were examined for size and quality using the Bioanalyzer High Sensitivity DNA Kit (Agilent) and cDNA concentrations were measured using the KAPA SYBR Fast qPCR kit (Roche). Samples were sequenced on an Illumina NovaSeq 6,000 instrument (paired end, read 1: 28 cycles, read 2: 90 cycles) with a targeted depth of 50,000 reads/cell.

scRNA-seq preprocessing, visualization, and clustering

In total, 8 thymus HAPC datasets were generated from 4 genotypes: Wild-type (WT) (n=2), *B2m*$^{-/-}$ (n=2), *MHCII*$^{-/-}$ (n=2), and *Rag2*$^{-/-}$ (n=2). Multiple cell clustering analyses were conducted using combinations of the samples and subsets of cells-of-interest (see below). scRNA-seq FASTQ reads were aligned to the C57BL/6J mm10 reference genome and quantified with Cell Ranger count version 6.0.1. [56]. Cell clustering and visualization analyses were performed using Seurat version 4.1.1 [57] in R version 4.2.2 (R Core Team, 2022).

We first analyzed WT HAPC scRNA-seq data to characterize the cellular heterogeneity of antigen presenting cells in the thymus of physiologically normal C57Bl/6J mice. Briefly, biological replicate samples were merged, and batch-corrected with 'FindIntegrationAnchors' and 'IntegrateData' Seurat functions. A minimum feature count/cell of 500, a maximum feature count/cell of 7000, and maximum mitochondrial content of 20% were specified as cutoffs. Next, we integrated all samples (n=8) to characterize cellular heterogeneity across genotypes. For WT and KO mice, samples were merged but not batch-corrected because variables-of-interest were confounded with

sequencing batch. A minimum feature count/cell of 1000, a maximum feature count/cell of 7000, and maximum mitochondrial content of 20% were used. For both WT-only and all sample integration analyses, cDCs were subset and re-analyzed separately from other cell types to characterize additional heterogeneity within the cDC compartment.

Expression counts were normalized using the 'NormalizeData' function and the top 2000 most variable genes were determined with 'FindVariableFeatures.' We then performed principal components analysis and used the top 30 principal components as input for k-nearest neighbor mapping and clustering using the 'FindNeighbors' and 'FindClusters' functions respectively. A resolution of 0.8 was used for clustering datasets initially, but a resolution of 1.5 was used to generate high resolution clusters for the merged samples. Finally, cells were projected into a UMAP dimension reduction with the 'RunUMAP' function.

For the WT hashtagged cDC dataset, FASTQ reads were aligned to the mm10 reference genome and quantified with Cell Ranger using the workflow for TotalSeqB samples [56]. Cell clustering and visualization analyses were performed using Seurat version 4.1.1 [57] in R version 4.2.2 (R Core Team, 2022). Hash-tagged oligo counts were processed with the "HTODemux" function in Seurat to assign cells to their respective subsets. Cells identified as doublets or negative for hashtag sequence counts were removed prior to gene expression analysis. Gene expression counts were then processed as described above with a minimum feature counts/cell of 1500, a maximum counts/cell of 7000, and a maximum mitochondrial content of 10%. Clusters identified from the hashtagged cDC dataset were annotated based on gene expression similarity to the original cDC dataset (Extended Data Fig. 1d).

Gene markers for each cDC cluster were calculated with the "FindAllMarkers' function, and gene expression analyses were performed with the 'FindMarkers' function,

using a minimum log-fold change of 0.25 and a minimum of 10% of cells within the cluster expressing the gene. Cell phase was calculated from expression data using the 'CellCycleScoring' function with default cell cycle genes provided in Seurat. Cell classes were then manually annotated for the calculated clusters based on curated lists of genes from Immgen database [58], Gene Expression Commons [59], and other relevant publications [10,19,44]. Cellxgene was used for scRNA-seq data visualization and exploration (https://github.com/chanzuckerberg/cellxgene).

scRNA-seq downstream analysis

For p-Creode analyses, Velocyto and scVelo (dynamic mode) were performed initially using the 10x Genomics BAM file from conventional dendritic cell (cDC) subsets, as documented previously [60–62]. Directionality converging to two activated cDC states enabled separation of the dataset into two distinct trajectories. p-Creode analysis was then carried out on data subsets as previously described [36]. Briefly, principal component analysis was conducted for dimension reduction while maintaining linearity in the data, and end states were identified in an unsupervised manner by closeness centrality value. Transition topologies were constructed using hierarchical placement, which iteratively connects end states and path nodes until the graph component is completed. Consensus topologies were then identified through resampled runs. RNA velocity vectors were visualized on top of the same UMAP embedding to delineate directionality of the transition through the topology. Ly6d^{+} cDCs were excluded from the trajectory due to their high transcriptional similarity to pDCs, suggesting a distinct origin[63]. MonoDC2s were excluded from the cDC2 trajectory because previous studies indicate they migrate to the thymus from the periphery and do not differentiate intrathymically[12,13].

To delineate genes whose dynamics are altered between the conditions (WT versus KO genotypes), tradeSeq[39] was applied to conduct conditionTest, which assesses differential expression patterns of the average gene expression with pairwise comparison between WT and knockout cDC1 and cDC2 trajectories. Gene set enrichment analysis[64,65] was performed on differentially expressed genes from tradeSeq to identify significantly enriched biological programs and pathways. A gene signature for each pathway was developed using the union lists of genes for pairwise comparisons (WT vs *B2m*$^{-/-}$, WT vs *MHC-II*$^{-/-}$, and WT vs *Rag2*$^{-/-}$) and signature score trends were computed by fitting generalized additive models (GAMs) over pseudotime. These trends were plotted as heatmaps with gene expression values normalized globally for all conditions.

For scRNA-seq correlation analyses with a published dataset, the top 200 gene markers for each cluster in each dataset were determined and combined into a gene list of common markers. Next, we calculated the average expression of all markers per cluster in each dataset and then calculated correlations between clusters using the spearman rank correlation. Correlations were then visualized as a heatmap using the 'pheatmap' package. For the union of genes identified by tradeSeq analysis per WT versus KO comparison for cDC1 and cDC2 trajectories, we performed functional enrichment analysis on the genes using the R package 'WebGestaltR' [66], and generated heatmaps showing gene expression for pathways of interest for UMAP-based cDC1, aDC1, cDC2, and aDC2 clusters.

Generation and analysis of Y-Ae bone marrow chimera mice

BM cells were isolated from the long bones of 6-week-old CD45.1 congenic mice. Bones were crushed and single cell suspensions were prepared in FWB, followed by red blood cells (RBC) lysis (RBC lysis buffer, Biolegend). Cells were stained with the

following lineage (Lin)-specific antibodies (all antibodies from BioXcell) - anti-CD11b (M1/70), anti-Gr-1 (RB6-8C5), anti-Ter-119 (TER-119), anti-B220 (RA3.3A1/6.1), anti-CD19 (1D3), anti-CD3 (17A2), and anti-CD8 (53.6.72). Lin^+ cells were depleted using sheep anti-rat IgG immunomagnetic beads (Dynabeads, Invitrogen). 8-10 x 10^6 Lin-depleted BM cells from CD45.1 congenic mice were retro-orbitally injected into 6-8-week-old lethally irradiated (1200 rads, delivered in 2 split doses separated by three hours) BALB/c and control B6 recipient mice. Mice were maintained on antibiotic feed (Teklad medicated diet, Inotiv, TD 06596) one day prior and 3 weeks after transplantation. Thymic DCs were analyzed by flow cytometry 8 weeks after reconstitution, including analysis of Y-Ae antibody binding to each DC subset.

Immunofluorescence of thymic sections

Thymi from C57Bl/6J, *MHC-II*$^{-/-}$, *B2m*$^{-/-}$ and *Rag2*$^{-/-}$ mice were snap-frozen in Tissue-Tek OCT (Sakura) and 7µm cryosections were generated with CryoStar™ NX50 cryostat (Thermo Fisher). Tissue sections were fixed in acetone for 20 minutes at -20°C. After fixation, tissue sections were rinsed with PBST thrice for 3 minutes each and then blocked with TNB (PerkinElmer) for 15 minutes at room temperature (RT). To determine $CD207^+$ cDC1 localization, slides were stained overnight (O/N) at 4°C with anti-CD207 (929F3.01, DENDRITICS), anti-CD11c-biotin (N418, Biolegend) and anti-XCR1-AF647 (ZET, BioLegend). Thymic slices were washed thrice at RT with PBST. Streptavidin-AF594 (Thermo Fisher) and Donkey anti-rat 488 (Jackson ImmunoResearch) were added for 1 hour at RT. To detect aDC1 or $CD14^+$ cDC2 subsets in the thymus, tissue sections were stained O/N 4°C with either anti-CD11c-biotin (N418, Biolegend), anti-CD63 (NVG-2, Biolegend) and anti-XCR1-AF647 (ZET, BioLegend) for aDC1s or anti-CD11c-biotin

(N418, Biolegend), anti-SIRPα (P84, Biolegend) and anti-CD14 (ab231852, Abcam) antibodies for $CD14^+$ cDC2s. For aDC1 stains, after washing, sections were then stained with Streptavidin-AF488 (Life Technologies) and Donkey anti-rat 594 (Jackson ImmunoResearch) for 1h at RT. For $CD14^+$ cDC2, sections were then stained with Streptavidin-AF488 (Life Technologies), Donkey anti-rat 594 (Jackson ImmunoResearch) and Donkey anti-rabbit 647 (Jackson ImmunoResearch) for 1 hour at RT. For staining aDC2 or pDC subsets, tissue sections were stained O/N 4°C with either anti-CD11c (N418, Biolegend) and anti-CD63 (NVG-2, Biolegend) for aDC2s or anti-CD11c (N418, Biolegend) and anti-SiglecH (552, Biolegend) for pDCs. Next, for aDC2 and pDC stains, sections were incubated with donkey anti-rat 594 (Jackson ImmunoResearch) for 1 hour at RT. Sections were then blocked with 2% rat serum at RT for 1 hour. Following blocking, anti-SIRPα-biotin (P84, Biolegend) was added, and slides were incubated for 1 hour at RT for aDC2s. Slides were incubated with anti-B220-biotin (RA3-6B2, Biolegend) for 1 hour at RT for the pDC stain. Next, slides for both aDC2 and pDC stains were washed and incubated with goat anti-armenian hamster 647 (Biolegend) and Streptavidin -AF488 (Life Technologies) for 1 hour at RT. To stain for macrophages, slides were stained with Mertk-APC (D5MMER, Invitrogen), CD63-PE-DazzleRed594 (NVG-2, Biolegend) and SIRPα-Biotin (P84, Biolegend) overnight at 4°C. The next day, slides were washed twice with PBS and once with PBST for 3 minutes each. Lastly, slides were incubated with Streptavidin- AF488 (Life Technologies) for 1hr at RT.

All slides were washed thrice with PBST before staining with DAPI and washing again. Slides were then mounted in ProLong™ Gold antifade reagent (Thermo Fisher) and imaged with a 20x and 40x objective on a DMi8 microscope (Leica).

Histocytometry

Histocytometry was based on analytical approaches previously described [67]. The entire thymus lobe was segmented using a Gaussian mixture model based on DAPI expression. Within this resulting region, another Gaussian mixture model using CD11c or CD63, where appropriate, was used to segment the medulla. Regions outside of the medulla were defined as the cortex. Manual adjustments were made in FIJI to remove imaging artifacts and correct misclassified areas. The CMJ region was then defined as the surrounding 50 µm on either side of the cortical-medullary boundary. After subtracting overlapping CMJ from both the medulla and cortex, the thymic regions were encoded one through three to create a unified mask. This mask was concatenated with the original images prior to cell segmentation, allowing the quantified single-cell data to include regional location.

To identify DC subsets and macrophages, a custom cell segmentation model using DAPI and CD11c or DAPI and CD63 fluorochrome expression was pre-trained on Cellpose [68]. Model fine-tuning was done using the Cellpose 2.0 GUI [69] and manual training input. Each DC subset was identified by a distinct combination of cell-surface markers (as in Fig. 1e and Extended Data Fig. 2g): $CD207^+$ cDC1 ($CD11c^+XCR1^+CD207^+$), CD14+ cDC2 ($CD11c^+SIRP\alpha^+CD14^+$), aDC1 ($CD11c^+XCR1^+CD63^+$), aDC2 ($CD11c^+SIRP\alpha^+CD63^+$), and pDC ($CD11c^+$ $SiglecH^+$ $B220^+$). For each cell, the median fluorochrome intensities for all channels and median encoded values for the thymic region mask were quantified using MCquant from the MCMICRO pipeline [70]. To ensure quality, cells were required to meet a minimum area threshold of 150 pixels or 71.74 um^2. Dendritic cell subsets were determined by manual gating via FlowJo. For each cDC subset, cellular density within each thymic region was calculated as the ratio of the number of cells in a given region to the area of that region in mm^2. To correct for macrophages included within identified aDC2s

($CD11c^+SIRP\alpha^+CD63^+$), the proportion of $CD63^+$ $SIRP\alpha^+$ $MerTK^-$ cells out of total $CD63^+$ $SIRP\alpha^+$ cells was calculated within each thymic region for three replicates. The median proportion of $CD63^+$ $SIRP\alpha^+$ $MerTK^-$ cells was multiplied by the initial aDC2 cell counts per thymic region to estimate the true aDC2 population without macrophages. Figures were generated with R 4.3.1 and Python.

Statistical analyses

All statistical tests were carried out using Prism (V9.2.0; GraphPad Software) and significance was determined using 1-way analysis of variance (ANOVA) with Tukey's multiple comparisons test/Dunnett's multiple comparisons test, or unpaired Student *t*-test, as indicated in the figure legends. $p < 0.05$ was considered significant: *$p < 0.05$; **$p < 0.01$; ***$p < 0.001$; ****$p < 0.0001$. Number of replicates and sample size for each experiment are included in the corresponding Figure legends. All statistical tests for histocytometry analysis were performed with R 4.3.1.

DATA AND CODE AVAILABILITY

scRNA-seq data have been deposited at the Gene Expression Omnibus (GEO: GSE239780). This study generated original code for histocytometry analyses, which can be found via Github (https://github.com/EhrlichLab/histocytometry_Srinivasan_2023). Scripts used for p-Creode analyses are available via Github (github.com/Ken-Lau-Lab/pCreode). Any additional information required to reanalyze the data reported in this paper is available upon request from the lead contact, Lauren I.R. Ehrlich (lehrlich@austin.utexas.edu).

REFERENCES

1. Ashby, K. M. & Hogquist, K. A. A guide to thymic selection of T cells. *Nat. Rev. Immunol.* (2023). doi:10.1038/s41577-023-00911-8
2. Ohnmacht, C. *et al.* Constitutive ablation of dendritic cells breaks self-tolerance of CD4 T cells and results in spontaneous fatal autoimmunity. *J. Exp. Med.* **206**, 549–559 (2009).
3. Březina, J., Vobořil, M. & Filipp, D. Mechanisms of Direct and Indirect Presentation of Self-Antigens in the Thymus. *Front. Immunol.* **13**, 1–13 (2022).
4. Li, J., Park, J., Foss, D. & Goldschneider, I. Thymus-homing peripheral dendritic cells constitute two of the three major subsets of dendritic cells in the steady-state thymus. *J. Exp. Med.* **206**, 607–622 (2009).
5. Wu, L. & Shortman, K. Heterogeneity of thymic dendritic cells. *Semin. Immunol.* **17**, 304–312 (2005).
6. Hu, Z. *et al.* CCR7 Modulates the Generation of Thymic Regulatory T Cells by Altering the Composition of the Thymic Dendritic Cell Compartment. *Cell Rep.* **21**, 168–180 (2017).
7. Ardouin, L. *et al.* Broad and Largely Concordant Molecular Changes Characterize Tolerogenic and Immunogenic Dendritic Cell Maturation in Thymus and Periphery. *Immunity* **45**, 305–318 (2016).
8. Oh, J. *et al.* CD40 Mediates Maturation of Thymic Dendritic Cells Driven by Self-Reactive CD4 + Thymocytes and Supports Development of Natural Regulatory T Cells. *J. Immunol.* **200**, 1399–1412 (2018).
9. Vobořil, M. *et al.* A model of preferential pairing between epithelial and dendritic cells in thymic antigen transfer. *Elife* **11**, 1–19 (2022).
10. Breed, E. R. *et al.* Type 2 cytokines in the thymus activate Sirpα+ dendritic cells to promote clonal deletion. *Nat. Immunol.* **23**, 1042–1051 (2022).
11. Vollmann, E. H. *et al.* Specialized transendothelial dendritic cells mediate thymic T-cell selection against blood-borne macromolecules. *Nat. Commun.* **12**, 1–19 (2021).
12. Zegarra-Ruiz, D. F. *et al.* Thymic development of gut-microbiota-specific T cells. *Nature* **594**, 413–417 (2021).
13. Vobořil, M. *et al.* Toll-like receptor signaling in thymic epithelium controls monocyte-derived dendritic cell recruitment and Treg generation. *Nat. Commun.* **11**, 2361 (2020).
14. Hadeiba, H. *et al.* Plasmacytoid Dendritic Cells Transport Peripheral Antigens to the Thymus to Promote Central Tolerance. *Immunity* **36**, 438–450 (2012).
15. Lopes, N., Charaix, J., Cédile, O., Sergé, A. & Irla, M. Lymphotoxin α fine-tunes T cell clonal deletion by regulating thymic entry of antigen-presenting cells. *Nat. Commun.* **9**, 1–16 (2018).
16. Baba, T., Nakamoto, Y. & Mukaida, N. Crucial Contribution of Thymic Sirpa+ Conventional Dendritic Cells to Central Tolerance against Blood-Borne Antigens

in a CCR2-Dependent Manner. *J. Immunol.* **183**, 3053–3063 (2009).
17. Spidale, N. A., Wang, B. & Tisch, R. Cutting Edge: Antigen-Specific Thymocyte Feedback Regulates Homeostatic Thymic Conventional Dendritic Cell Maturation. *J. Immunol.* **193**, 21–25 (2014).
18. Guilliams, M. *et al.* Unsupervised High-Dimensional Analysis Aligns Dendritic Cells across Tissues and Species. *Immunity* **45**, 669–684 (2016).
19. Zilionis, R. *et al.* Single-Cell Transcriptomics of Human and Mouse Lung Cancers Reveals Conserved Myeloid Populations across Individuals and Species. *Immunity* **50**, 1317-1334.e10 (2019).
20. Eferl, R. & Wagner, E. F. AP-1: a double-edged sword in tumorigenesis. *Nat. Rev. Cancer* **3**, 859–868 (2003).
21. Lancaster, J. N., Li, Y. & Ehrlich, L. I. R. Chemokine-Mediated Choreography of Thymocyte Development and Selection. *Trends Immunol.* **39**, 86–98 (2018).
22. Zhou, T.-A. *et al.* Thymic macrophages consist of two populations with distinct localization and origin. *Elife* **11**, 2021.11.04.467238 (2022).
23. Li, Y. *et al.* CCR4 and CCR7 differentially regulate thymocyte localization with distinct outcomes for central tolerance. *Elife* **12**, 1–30 (2023).
24. Daley, S. R., Hu, D. Y. & Goodnow, C. C. Helios marks strongly autoreactive CD4+ T cells in two major waves of thymic deletion distinguished by induction of PD-1 or NF-κB. *J. Exp. Med.* **210**, 269–285 (2013).
25. Stritesky, G. L. *et al.* Murine thymic selection quantified using a unique method to capture deleted T cells. *Proc. Natl. Acad. Sci.* **110**, 4679–4684 (2013).
26. Kurts, C. *et al.* Constitutive class I-restricted exogenous presentation of self antigens in vivo. *J. Exp. Med.* **184**, 923–930 (1996).
27. Kurts, C., Miller, J. F. A. P., Subramaniam, R. M., Carbone, F. R. & Heath, W. R. Major Histocompatibility Complex Class I–restricted Cross-presentation Is Biased towards High Dose Antigens and Those Released during Cellular Destruction. *J. Exp. Med.* **188**, 409–414 (1998).
28. Humblet, C., Rudensky, A. Y. & Kyewski, B. Presentation and intercellular transfer of self antigen within the thymic microenvironment: expression of the Eα peptide-l-A b complex by isolated thymic stromal cells. *Int. Immunol.* **6**, 1949–1958 (1994).
29. Owen, D. L. *et al.* Thymic regulatory T cells arise via two distinct developmental programs. *Nat. Immunol.* **20**, 195–205 (2019).
30. Proietto, A. I. *et al.* Dendritic cells in the thymus contribute to T-regulatory cell induction. *Proc. Natl. Acad. Sci. U. S. A.* **105**, 19869–74 (2008).
31. Roche, P. A. & Furuta, K. The ins and outs of MHC class II-mediated antigen processing and presentation. *Nat. Rev. Immunol.* **15**, 203–216 (2015).
32. Watanabe, M., Lu, Y., Breen, M. & Hodes, R. J. B7-CD28 co-stimulation modulates central tolerance via thymic clonal deletion and Treg generation through distinct mechanisms. *Nat. Commun.* **11**, 6264 (2020).
33. Laurent, J., Bosco, N., Marche, P. N. & Ceredig, R. New insights into the proliferation and differentiation of early mouse thymocytes. *Int. Immunol.* **16**,

1069–1080 (2004).
34. Mombaerts, P. *et al.* Mutations in T-cell antigen receptor genes α and β block thymocyte development at different stages. *Nature* **360**, 225–231 (1992).
35. Edilova, M. I., Abdul-Sater, A. A. & Watts, T. H. TRAF1 Signaling in Human Health and Disease. *Front. Immunol.* **9**, 1–12 (2018).
36. Herring, C. A. *et al.* Unsupervised Trajectory Analysis of Single-Cell RNA-Seq and Imaging Data Reveals Alternative Tuft Cell Origins in the Gut. *Cell Syst.* **6**, 37-51.e9 (2018).
37. Gulati, G. S. *et al.* Single-cell transcriptional diversity is a hallmark of developmental potential. *Science (80-.).* **367**, 405–411 (2020).
38. Wu, R. & Murphy, K. M. DCs at the center of help: Origins and evolution of the three-cell-type hypothesis. *J. Exp. Med.* **219**, 1–13 (2022).
39. Van den Berge, K. *et al.* Trajectory-based differential expression analysis for single-cell sequencing data. *Nat. Commun.* **11**, 1–13 (2020).
40. Hikosaka, Y. *et al.* The Cytokine RANKL Produced by Positively Selected Thymocytes Fosters Medullary Thymic Epithelial Cells that Express Autoimmune Regulator. *Immunity* **29**, 438–450 (2008).
41. Hoesel, B. & Schmid, J. A. The complexity of NF-κB signaling in inflammation and cancer. *Mol. Cancer* **12**, 86 (2013).
42. Sun, S. C. The non-canonical NF-κB pathway in immunity and inflammation. *Nat. Rev. Immunol.* **17**, 545–558 (2017).
43. Ferris, S. T. *et al.* cDC1 prime and are licensed by CD4+ T cells to induce anti-tumour immunity. *Nature* **584**, 624–629 (2020).
44. Park, J.-E. *et al.* A cell atlas of human thymic development defines T cell repertoire formation. *Science (80-.).* **367**, (2020).
45. Perry, J. S. A. *et al.* CD36 Mediates Cell-Surface Antigens to Promote Thymic Development of the Regulatory T Cell Receptor Repertoire and Allo-tolerance. *Immunity* **48**, 923–936 (2018).
46. Herbin, O. *et al.* Medullary thymic epithelial cells and CD8α+dendritic cells coordinately regulate central tolerance but CD8α+cells are dispensable for thymic regulatory T cell production. *J. Autoimmun.* **75**, 141–149 (2016).
47. Perry, J. S. A. *et al.* Distinct Contributions of Aire and Antigen-Presenting-Cell Subsets to the Generation of Self-Tolerance in the Thymus. *Immunity* **41**, 414–426 (2014).
48. Gallucci, S., Lolkema, M. & Matzinger, P. Natural adjuvants: Endogenous activators of dendritic cells. *Nat. Med.* **5**, 1249–1255 (1999).
49. Montoya, M. *et al.* Type I interferons produced by dendritic cells promote their phenotypic and functional activation. *Blood* **99**, 3263–3271 (2002).
50. Benhammadi, M. *et al.* IFN-λ Enhances Constitutive Expression of MHC Class I Molecules on Thymic Epithelial Cells. *J. Immunol.* **205**, 1268–1280 (2020).
51. Lienenklaus, S. *et al.* Novel Reporter Mouse Reveals Constitutive and Inflammatory Expression of IFN-β In Vivo. *J. Immunol.* **183**, 3229–3236 (2009).
52. Joyee, A. G., Uzonna, J. & Yang, X. Invariant NKT Cells Preferentially Modulate

the Function of CD8α+ Dendritic Cell Subset in Inducing Type 1 Immunity against Infection. *J. Immunol.* **184**, 2095–2106 (2010).
53. Pasqual, G. *et al.* Monitoring T cell-dendritic cell interactions in vivo by intercellular enzymatic labelling. *Nature* **553**, 496–500 (2018).
54. Park, S.-J. *et al.* IL-6 Regulates In Vivo Dendritic Cell Differentiation through STAT3 Activation. *J. Immunol.* **173**, 3844–3854 (2004).
55. Seach, N., Wong, K., Hammett, M., Boyd, R. L. & Chidgey, A. P. Purified enzymes improve isolation and characterization of the adult thymic epithelium. *J. Immunol. Methods* **385**, 23–34 (2012).
56. Zheng, G. X. Y. *et al.* Massively parallel digital transcriptional profiling of single cells. *Nat. Commun.* **8**, (2017).
57. Hao, Y. *et al.* Integrated analysis of multimodal single-cell data. *Cell* **184**, 3573-3587.e29 (2021).
58. Miller, J. C. *et al.* Deciphering the transcriptional network of the dendritic cell lineage. *Nat. Immunol.* **13**, 888–899 (2012).
59. Seita, J. *et al.* Gene expression commons: An open platform for absolute gene expression profiling. *PLoS One* **7**, 1–11 (2012).
60. Chen, B. *et al.* Differential pre-malignant programs and microenvironment chart distinct paths to malignancy in human colorectal polyps. *Cell* **184**, 6262-6280.e26 (2021).
61. Bergen, V., Lange, M., Peidli, S., Wolf, F. A. & Theis, F. J. Generalizing RNA velocity to transient cell states through dynamical modeling. *Nat. Biotechnol.* **38**, 1408–1414 (2020).
62. La Manno, G. *et al.* RNA velocity of single cells. *Nature* **560**, 494–498 (2018).
63. Lutz, K. *et al.* Ly6D+Siglec-H+ precursors contribute to conventional dendritic cells via a Zbtb46+Ly6D+ intermediary stage. *Nat. Commun.* **13**, 1–15 (2022).
64. Subramanian, A. *et al.* Gene set enrichment analysis: A knowledge-based approach for interpreting genome-wide expression profiles. *Proc. Natl. Acad. Sci. U. S. A.* **102**, 15545–15550 (2005).
65. Mootha, V. K. *et al.* PGC-1α-responsive genes involved in oxidative phosphorylation are coordinately downregulated in human diabetes. *Nat. Genet.* **34**, 267–273 (2003).
66. Wang, J., Vasaikar, S., Shi, Z., Greer, M. & Zhang, B. WebGestalt 2017: a more comprehensive, powerful, flexible and interactive gene set enrichment analysis toolkit. *Nucleic Acids Res.* **45**, W130–W137 (2017).
67. Gerner, M. Y., Kastenmuller, W., Ifrim, I., Kabat, J. & Germain, R. N. Histo-cytometry: a method for highly multiplex quantitative tissue imaging analysis applied to dendritic cell subset microanatomy in lymph nodes. *Immunity* **37**, 364–76 (2012).
68. Stringer, C., Wang, T., Michaelos, M. & Pachitariu, M. Cellpose: a generalist algorithm for cellular segmentation. *Nat. Methods* **18**, 100–106 (2021).
69. Pachitariu, M. & Stringer, C. Cellpose 2.0: how to train your own model. *Nat. Methods* **19**, 1634–1641 (2022).

70. Schapiro, D. *et al*. MCMICRO: a scalable, modular image-processing pipeline for multiplexed tissue imaging. *Nat. Methods* **19**, 311–315 (2022).

FIGURES AND FIGURE LEGENDS

Figure 1

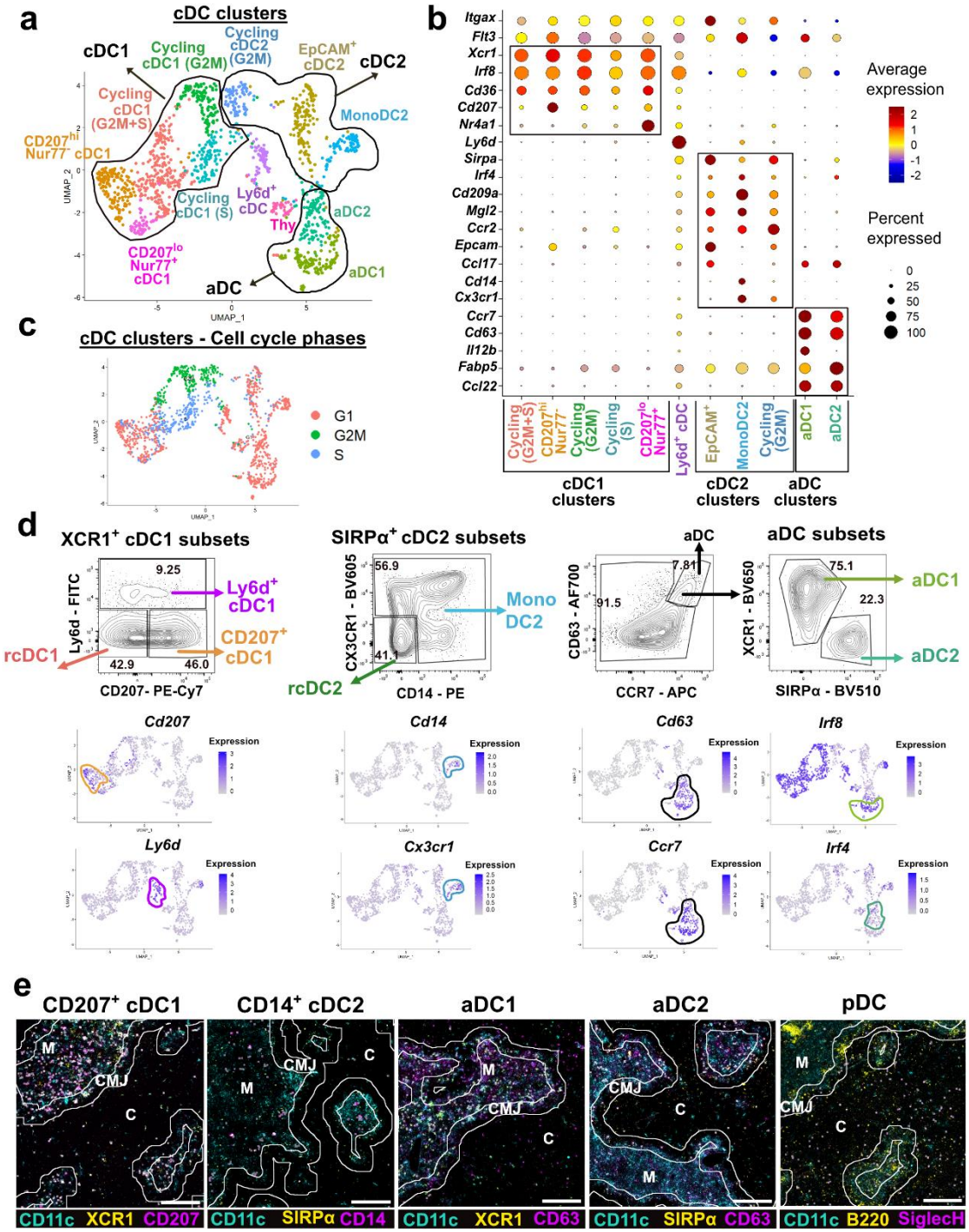

Figure 1. scRNA-seq reveals transcriptional heterogeneity in the thymic DC compartment

(a) UMAP visualization of 1399 re-clustered thymic cDCs from adult C57BL/6J (WT) mice (n=2) depicting 11 transcriptionally distinct cDC clusters. (b) Normalized expression (z-score) of select DC marker genes across the transcriptionally defined cDC clusters from (a). (c) Cell-cycle phases across the cDC clusters from (a). (d) (Top) Representative flow cytometry plots identifying 7 distinct cDC subsets based on protein expression of cluster-specific genes (gating strategy in Extended Data Fig. 2a). (Bottom) Expression levels of cDC cluster-specific genes for the respective flow-defined subsets above. (e) Representative immunofluorescence used to quantify locations of the indicated DC subsets in thymic sections (representative of N=3 independent experiments). Scale bar, 250µm. Lines demarcate the cortex (C), medulla (M), and CMJ in each thymic section. Centroids were overlaid on cells meeting the criteria for each indicated cDC subset (see Methods). See also Extended Data Fig. 1 and 2.

Figure 2

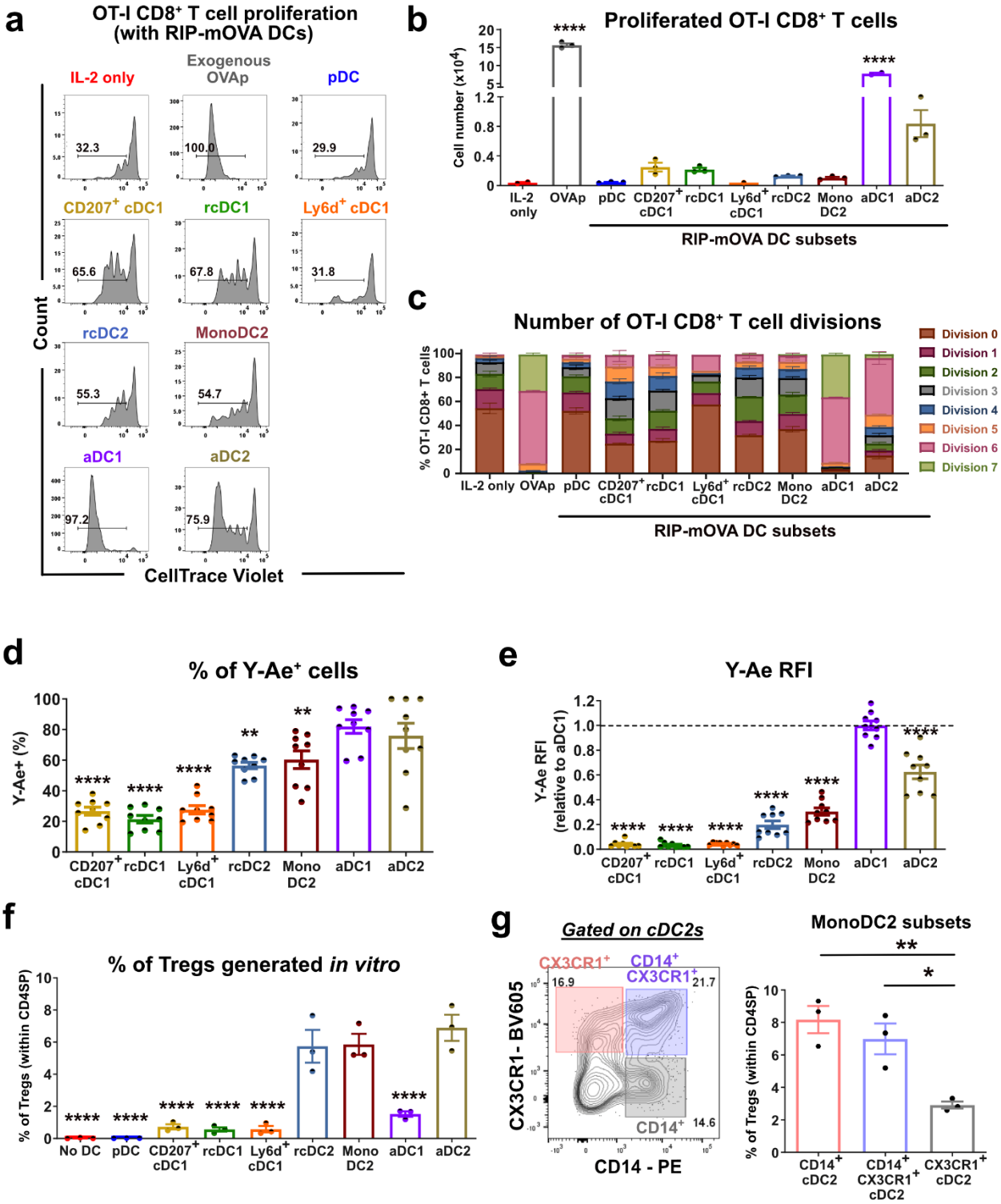
a
OT-I CD8+ T cell proliferation (with RIP-mOVA DCs)
IL-2 only
Exogenous OVAp
pDC
CD207+ cDC1
rcDC1
Ly6d+ cDC1
rcDC2
MonoDC2
aDC1
aDC2
32.3
100.0
29.9
65.6
67.8
31.8
55.3
54.7
97.2
75.9
Count
CellTrace Violet
b
Proliferated OT-I CD8+ T cells
Cell number (x10^4)
IL-2 only
OVAp
pDC
CD207+ cDC1
rcDC1
Ly6d+ cDC1
rcDC2
Mono DC2
aDC1
aDC2
RIP-mOVA DC subsets
c
Number of OT-I CD8+ T cell divisions
% OT-I CD8+ T cells
Division 0
Division 1
Division 2
Division 3
Division 4
Division 5
Division 6
Division 7
RIP-mOVA DC subsets
d
% of Y-Ae+ cells
Y-Ae+ (%)
e
Y-Ae RFI
Y-Ae RFI (relative to aDC1)
f
% of Tregs generated in vitro
% of Tregs (within CD4SP)
No DC
g
Gated on cDC2s
CX3CR1+
CD14+ CX3CR1+
CD14+
CX3CR1- BV605
CD14 - PE
MonoDC2 subsets
CD14+ cDC2
CD14+ CX3CR1+ cDC2
CX3CR1+ cDC2

Figure 2. cDC subsets have distinct abilities to present antigens and induce Treg differentiation

(a) Representative histograms showing the percentage of OT-I $CD8^+$ T cells that underwent at least 1 cell division after co-culture for 3.5 days with the specified DC subsets from RIP-mOVA mice. OT-I $CD8^+$ T cells incubated only with IL-2 served as negative controls, while those co-cultured with splenocytes pulsed with 50nM of SIINFEKLp (OVAp) served as positive controls. For (a-c), data are representative of 3 independent experiments. (b) Quantification of OT-I $CD8^+$ T cells that underwent proliferation from the experiment in (a). Bars represent mean ± SEM. Each dot represents a replicate well. (c) Modeling, based on the experiment in (a), of the frequency of OT-I $CD8^+$ T cells that underwent the indicated number of cell divisions. Bars represent mean ± SEM. (d) Frequency of Y-Ae^+ cells and (e) relative fluorescence intensity (RFI) of Y-Ae expression on C57BL/6J donor-derived thymic cDC subsets from BM chimeras of C57BL/6J hematopoietic progenitors transplanted into lethally irradiated BALB/c mice. (d-e) Data are compiled from N= 3 independent experiments (n=9 mice total). Bars represent mean ± SEM and symbols represent individual mice. (e) Data are normalized to the average Y-Ae MFI of aDC1s in each individual experiment. (f) Percentage of $Foxp3^+$ $CD25^+$ Tregs induced after culture of $CD73^-$ $CD25^-$ $Foxp3^-$ CD4SP thymocytes with the indicated C57BL/6J thymic DC subsets for 4 days. (f-g) Data are compiled from N= 3 independent experiments. Bars represent mean ± SEM and symbols represent average of triplicate wells per DC subset from each experiment. (g) (Left) Representative flow cytometry plot depicting the three heterogenous subpopulations within MonoDC2s. (Right) Percentage of Tregs induced by each MonoDC2 subpopulation in an in vitro Treg generation assay, as in (f). Statistical analysis was performed using one-way ANOVA with (b, d, e, and f) Dunnett's multiple comparisons test and (g) Tukey's multiple comparisons test; *$p<0.05$, ** $p<0.01$, ****$p<0.0001$. Significance is relative to (b) "IL-2 only" control, (d and e) aDC1 subset, and (f) aDC2 subset.
See also Extended Data Fig. 3.

Figure 3

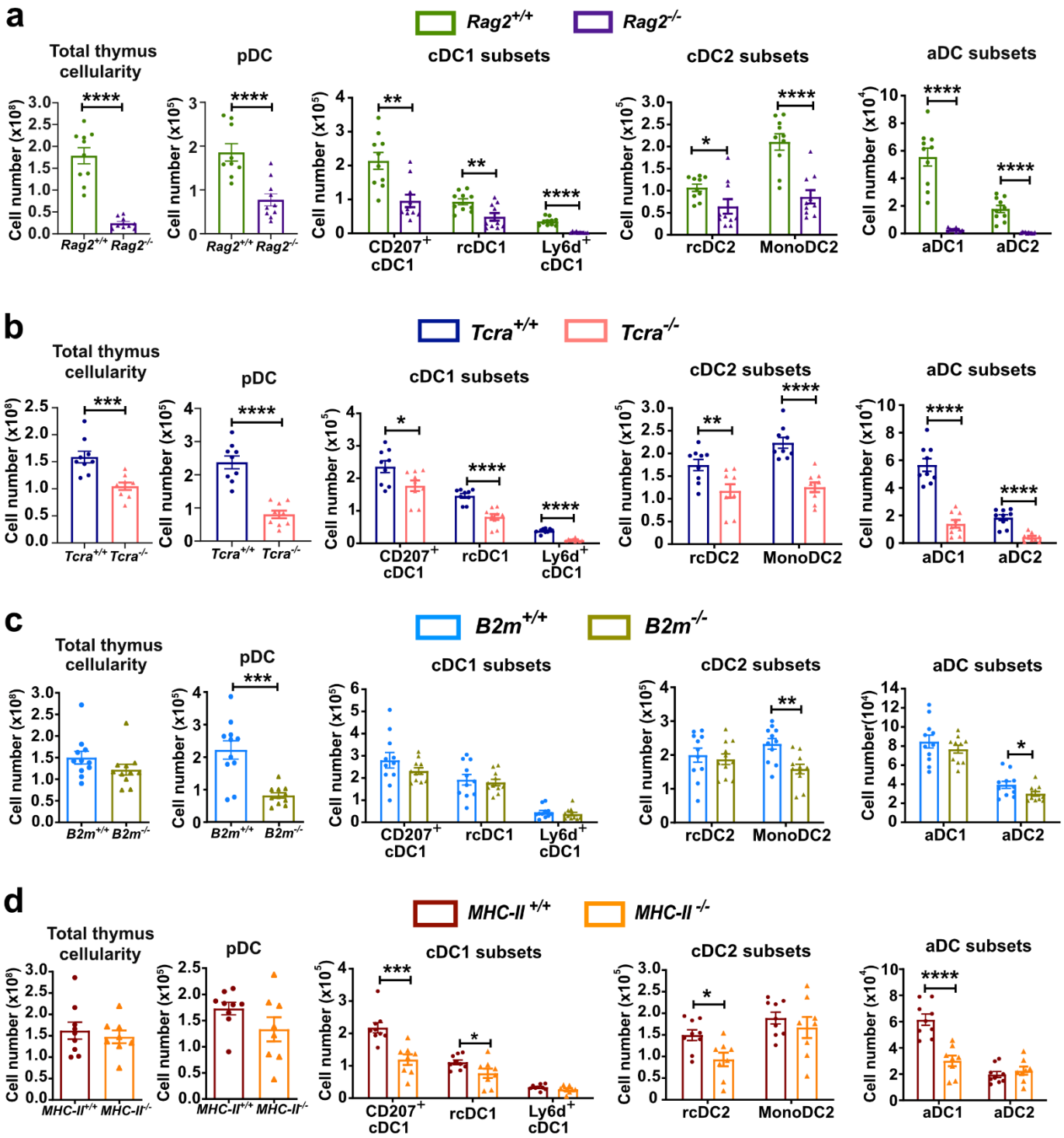
a
Rag2+/+
Rag2-/-
Total thymus cellularity
pDC
cDC1 subsets
cDC2 subsets
aDC subsets
Cell number (x10^8)
Cell number (x10^5)
Cell number (x10^4)
Rag2+/+ Rag2-/-
CD207+ cDC1
rcDC1
Ly6d+ cDC1
rcDC2
MonoDC2
aDC1
aDC2
b
Tcra+/+
Tcra-/-
Tcra+/+ Tcra-/-
c
B2m+/+
B2m-/-
B2m+/+ B2m-/-
Cell number(10^4)
d
MHC-II +/+
MHC-II -/-
MHC-II+/+ MHC-II-/-

Figure 3. Thymic cDC1 and cDC2 homeostasis and activation depend on the presence of distinct thymocyte subsets

(a-d) Quantification of (left to right) total thymus cellularity and cell numbers of pDCs, cDC1 subsets, cDC2 subsets, and aDC subsets from the thymi of WT versus (a) *Rag2*$^{-/-}$, (b) *Tcra*$^{-/-}$, (c) *B2m*$^{-/-}$ and (d) *MHC-II*$^{-/-}$ littermate mice. Data are compiled from N=3-4 independent experiments (n=8-11 mice). Bars represent mean ± SEM and symbols represent individual mice. Statistical analysis was performed using unpaired Student *t*-test; *p<0.05, ** p<0.01, ***p<0.001, ****p<0.0001.
See also Extended Data Fig. 4.

Figure 4

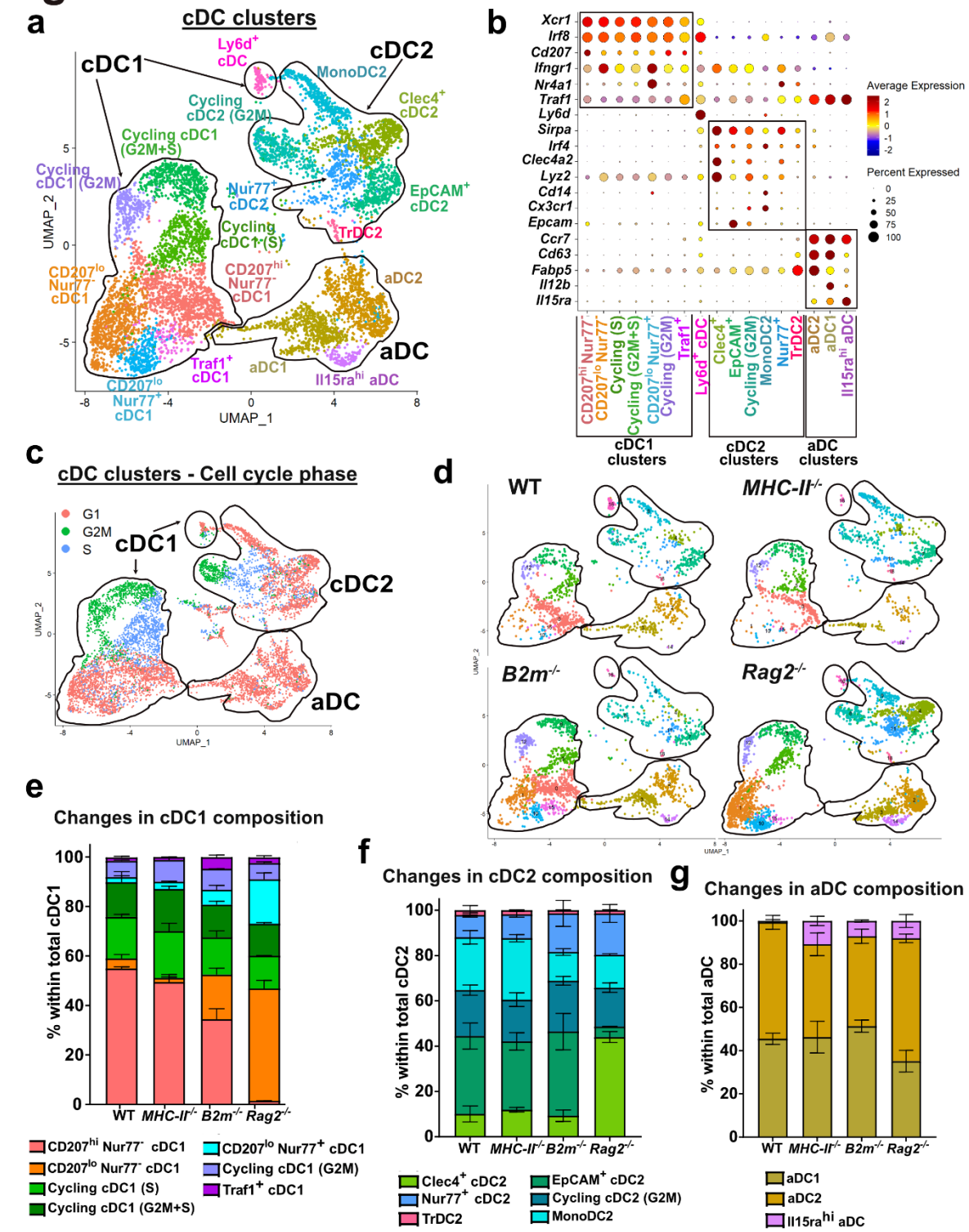
a
cDC clusters
cDC1
cDC2
Ly6d+ cDC
MonoDC2
Cycling cDC2 (G2M)
Clec4+ cDC2
Cycling cDC1 (G2M+S)
Cycling cDC1 (G2M)
Nur77+ cDC2
EpCAM+ cDC2
Cycling cDC1 (S)
TrDC2
CD207lo Nur77- cDC1
CD207hi Nur77- cDC1
aDC2
aDC
Traf1+ cDC1
aDC1
Il15rahi aDC
CD207lo Nur77+ cDC1
UMAP_1
UMAP_2
b
Xcr1
Irf8
Cd207
Ifngr1
Nr4a1
Traf1
Ly6d
Sirpa
Irf4
Clec4a2
Lyz2
Cd14
Cx3cr1
Epcam
Ccr7
Cd63
Fabp5
Il12b
Il15ra
Average Expression
Percent Expressed
cDC1 clusters
cDC2 clusters
aDC clusters
c
cDC clusters - Cell cycle phase
G1
G2M
S
cDC1
cDC2
aDC
d
WT
MHC-II-/-
B2m-/-
Rag2-/-
e
Changes in cDC1 composition
% within total cDC1
WT
MHC-II-/-
B2m-/-
Rag2-/-
CD207hi Nur77- cDC1
CD207lo Nur77- cDC1
Cycling cDC1 (S)
Cycling cDC1 (G2M+S)
CD207lo Nur77+ cDC1
Cycling cDC1 (G2M)
Traf1+ cDC1
f
Changes in cDC2 composition
% within total cDC2
Clec4+ cDC2
Nur77+ cDC2
TrDC2
EpCAM+ cDC2
Cycling cDC2 (G2M)
MonoDC2
g
Changes in aDC composition
% within total aDC
aDC1
aDC2
Il15rahi aDC

Figure 4. scRNA-seq profiling identifies the emergence of unique DC transcriptional states in the absence of thymocyte crosstalk

(a) Merged UMAP representation of 7982 reclustered cDCs from WT, *MHC-II*$^{-/-}$, *B2m*$^{-/-}$ and *Rag2*$^{-/-}$ thymi (n=2 mice per genotype). (b) Dot plots showing normalized expression (z-score) of cDC1-, cDC2- and aDC-specific genes across cDC clusters from (a). (c) Cell-cycle phase analysis for cDC clusters from (a). (d) UMAP representation of cDC clusters from (a), separated by genotype of origin. (e-g) Frequency of transcriptionally distinct (e) cDC1 clusters, (f) cDC2 clusters, and (g) aDC clusters shown in (a), within the parent population indicated on the Y-axis label separated by the indicated genotypes (n=2 mice per genotype). Bars represent mean ± SEM.
See also Extended Data Fig. 5.

Figure 5

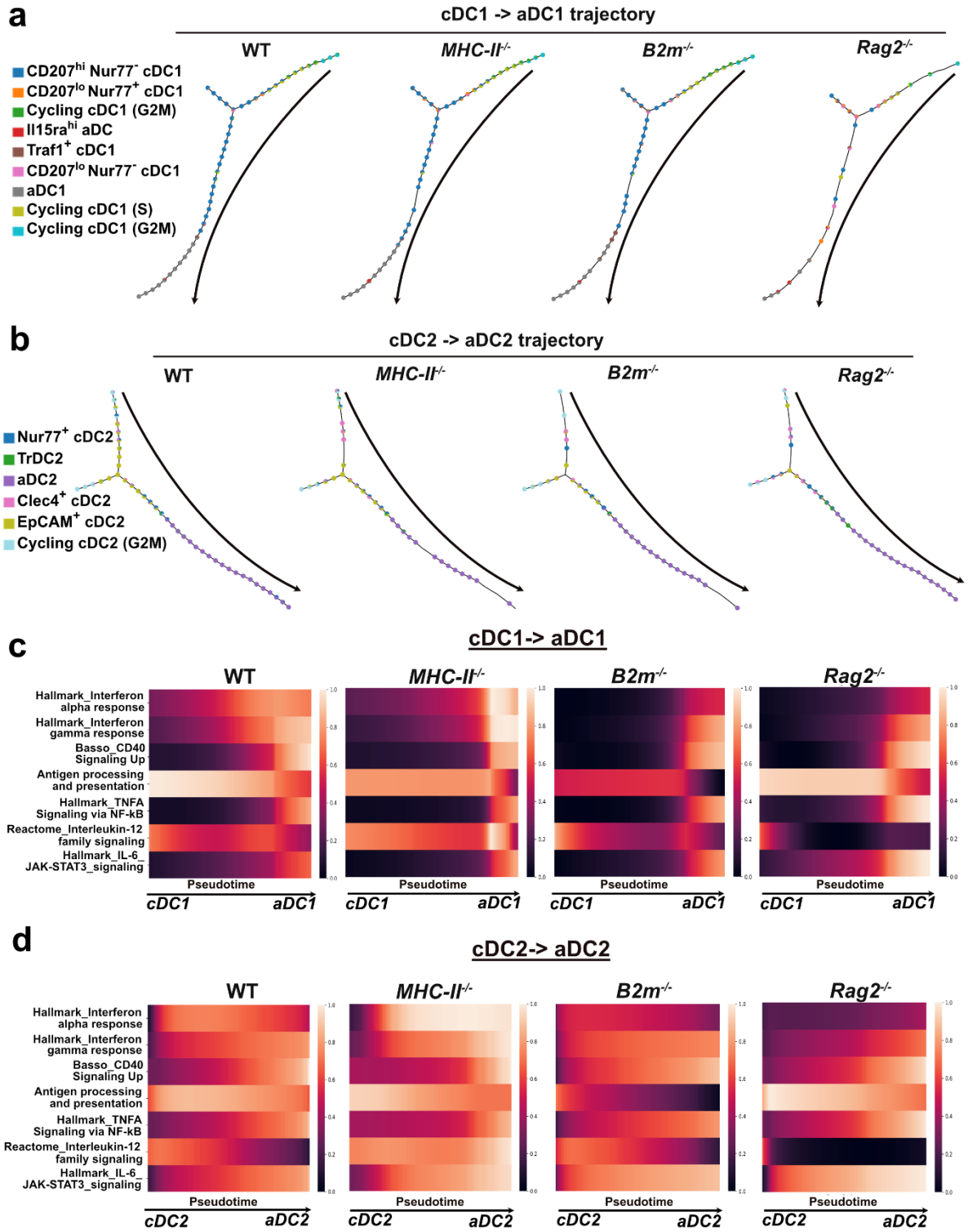
a
cDC1 -> aDC1 trajectory
WT
MHC-II-/-
B2m-/-
Rag2-/-
CD207hi Nur77- cDC1
CD207lo Nur77+ cDC1
Cycling cDC1 (G2M)
Il15rahi aDC
Traf1+ cDC1
CD207lo Nur77- cDC1
aDC1
Cycling cDC1 (S)
Cycling cDC1 (G2M)
b
cDC2 -> aDC2 trajectory
WT
MHC-II-/-
B2m-/-
Rag2-/-
Nur77+ cDC2
TrDC2
aDC2
Clec4+ cDC2
EpCAM+ cDC2
Cycling cDC2 (G2M)
c
cDC1-> aDC1
WT
MHC-II-/-
B2m-/-
Rag2-/-
Hallmark_Interferon alpha response
Hallmark_Interferon gamma response
Basso_CD40 Signaling Up
Antigen processing and presentation
Hallmark_TNFA Signaling via NF-kB
Reactome_Interleukin-12 family signaling
Hallmark_IL-6_ JAK-STAT3_signaling
Pseudotime
cDC1
aDC1
d
cDC2-> aDC2
WT
MHC-II-/-
B2m-/-
Rag2-/-
Hallmark_Interferon alpha response
Hallmark_Interferon gamma response
Basso_CD40 Signaling Up
Antigen processing and presentation
Hallmark_TNFA Signaling via NF-kB
Reactome_Interleukin-12 family signaling
Hallmark_IL-6_ JAK-STAT3_signaling
Pseudotime
cDC2
aDC2

Figure 5. SP thymocytes contribute to DC homeostasis and activation by regulating interferon signaling and NF-kB signaling

(a-b) p-Creode topology depicting transcriptional states (represented as nodes) along the (a) cDC1 and (b) cDC2 differentiation trajectories. The colors in each node represent the proportion of cDC1 and cDC2 transcriptional clusters from Fig. 4a comprising each respective transcriptional state. (c-d) Pseudotime heatmaps displaying signature scores of pathways associated with genes that were differentially expressed along the (c) cDC1–aDC1 and (d) cDC2-aDC2 differentiation trajectories for each WT versus KO comparison. See also Extended Data Fig. 6 and 7.

Figure 6

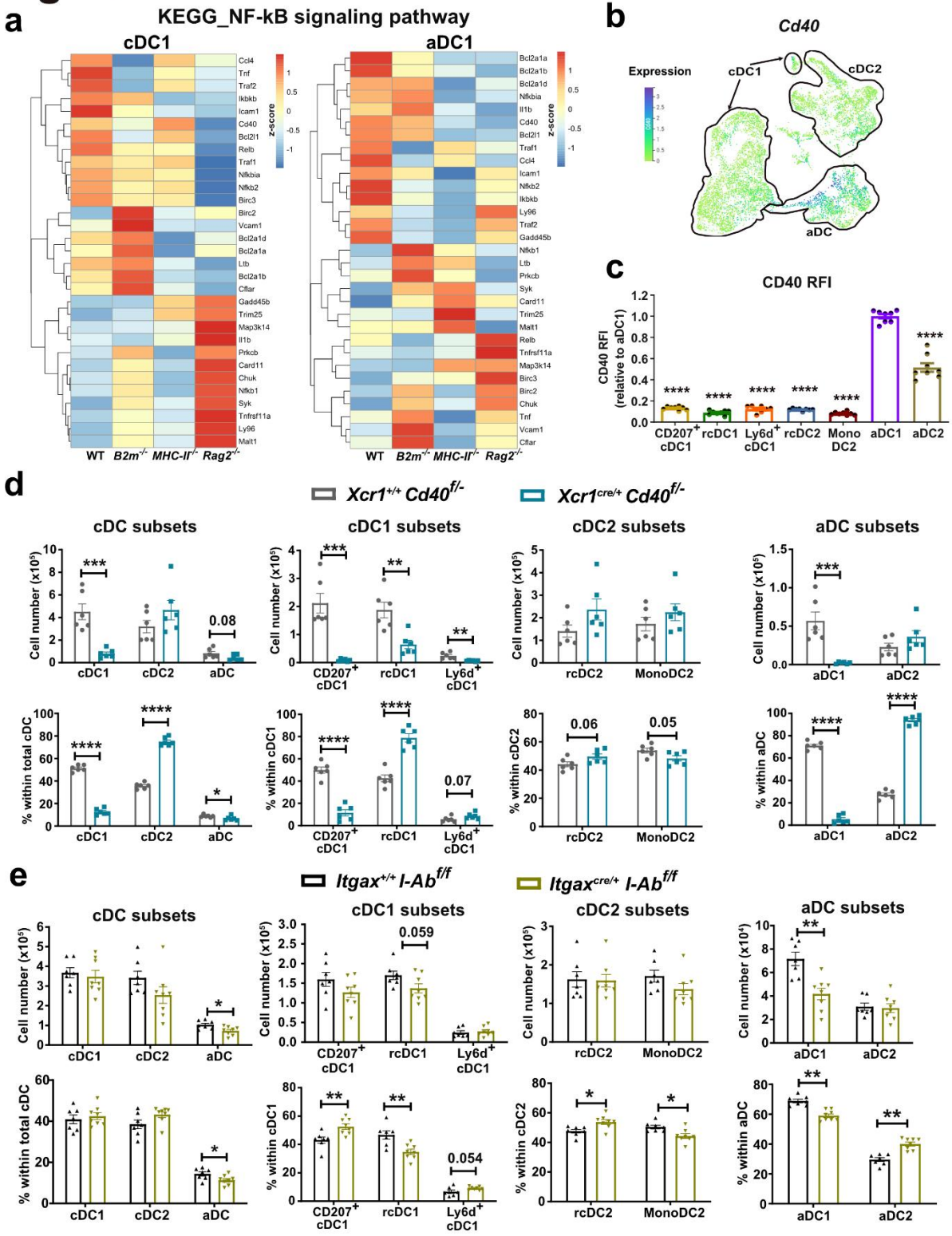
a
KEGG_NF-kB signaling pathway
cDC1
aDC1
z-score
WT
B2m-/-
MHC-II-/-
Rag2-/-
b
Cd40
Expression
cDC1
cDC2
aDC
c
CD40 RFI
CD40 RFI (relative to aDC1)
CD207+ cDC1
rcDC1
Ly6d+ cDC1
rcDC2
Mono DC2
aDC1
aDC2
d
Xcr1+/+ Cd40f/-
Xcr1cre/+ Cd40f/-
cDC subsets
cDC1 subsets
cDC2 subsets
aDC subsets
Cell number (x10^5)
% within total cDC
% within cDC1
% within cDC2
% within aDC
e
Itgax+/+ I-Abf/f
Itgax cre/+ I-Abf/f
Cell number (x10^4)

Figure 6. Cognate interactions with CD4SP thymocytes and CD40-CD40L interactions are differentially required for cDC1 homeostasis and activation

(a) Heatmaps show normalized expression (z-score) of individual genes associated with the KEGG_NF-kB signaling pathway that were differentially regulated along the DC differentiation trajectories (as in Fig. 5c-d) of (left) cDC1s and (right) aDC1s from pairwise comparisons of WT versus *B2m*$^{-/-}$, *MHC-II*$^{-/-}$ or *Rag2*$^{-/-}$ datasets. (b) *Cd40* gene expression levels overlaid on the UMAP representation of scRNA-seq datasets from WT and KO thymic cDCs, as in Fig. 4a. (c) CD40 RFI levels in flow cytometry-defined cDC subsets. Data are normalized to average MFI levels of aDC1s per experimental repeat. (d-e) Quantification of frequency and cell numbers of (left to right) total cDC, cDC1, cDC2, and aDC subsets in (d) *Xcr1*$^{+/+}$ *Cd40*$^{f/-}$ versus *Xcr1*$^{cre/+}$ *Cd40*$^{f/-}$ littermate mice and (e) *Itgax*$^{+/+}$ *I-Ab*$^{f/f}$ versus *Itgax*$^{cre/+}$ *I-Ab*$^{f/f}$ littermate mice. (c-e) Data are compiled from N=3 independent experiments (n=6-8 mice). Bars represent mean ± SEM and symbols represent individual mice. Statistical analysis was performed using (c) one-way ANOVA with Dunnett's multiple comparisons test and (d-e) unpaired Student *t*-test; *p<0.05, ** p<0.01, ***p<0.001, ****p<0.0001. (c) Significance is relative to aDC1 subset.

See also Extended Data Fig. 7.

EXTENDED DATA

Extended Data Figure 1

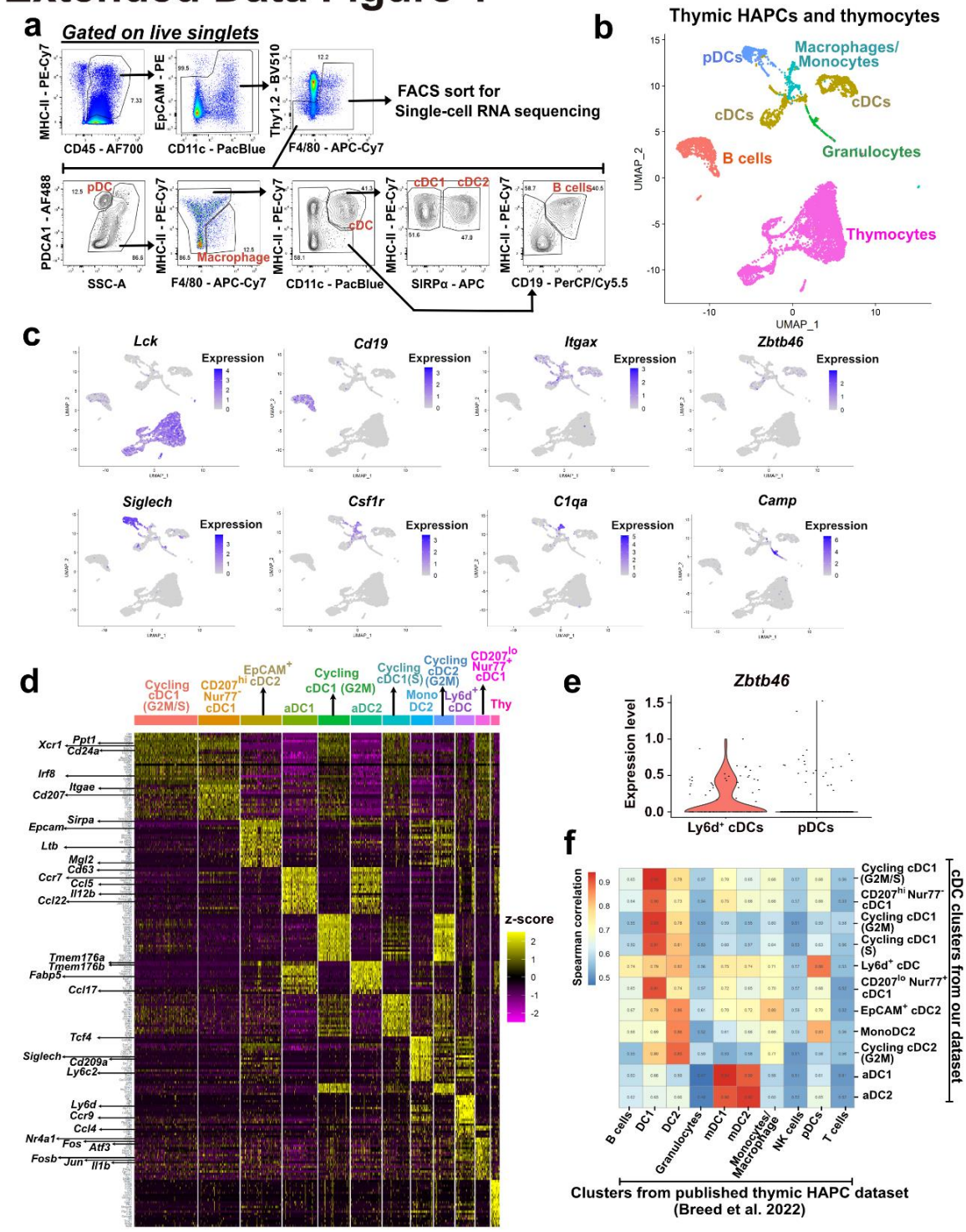

Extended Data Fig. 1. Identification of transcriptionally distinct HAPC subsets, related to Fig. 1.

(a) Flow cytometric gating strategy used to sort HAPCs for scRNA-seq analysis. (b) UMAP visualization showing major HAPC populations identified from 8404 FACS-sorted HAPCs (and residual thymocytes) from adult C57BL6/J thymi- B cells (*Cd19*), cDCs (*Zbtb46*, *Itgax*), pDCs (*Itgax*, *Siglech*), macrophages/monocytes (*Csf1r*, *C1qa*), granulocytes (*Camp*), and thymocytes (*Lck*). (c) Feature plots showing expression levels of select genes associated with the major HAPC subsets overlaid on the UMAP visualization from (b). (d) Heatmap displaying normalized expression of the top 10 differentially expressed genes in each transcriptionally distinct cDC cluster from Fig. 1a. Arrows highlight select genes specific to the transcriptionally distinct cDC1, cDC2, and aDC clusters. (e) Violin plot displaying normalized expression levels of *Zbtb46* gene in Ly6d^{+} cDCs and pDCs. (f) Spearman correlation analysis of thymic cDC clusters from our dataset, and cDC and other clusters in the dataset from[10].

Extended Data Figure 2

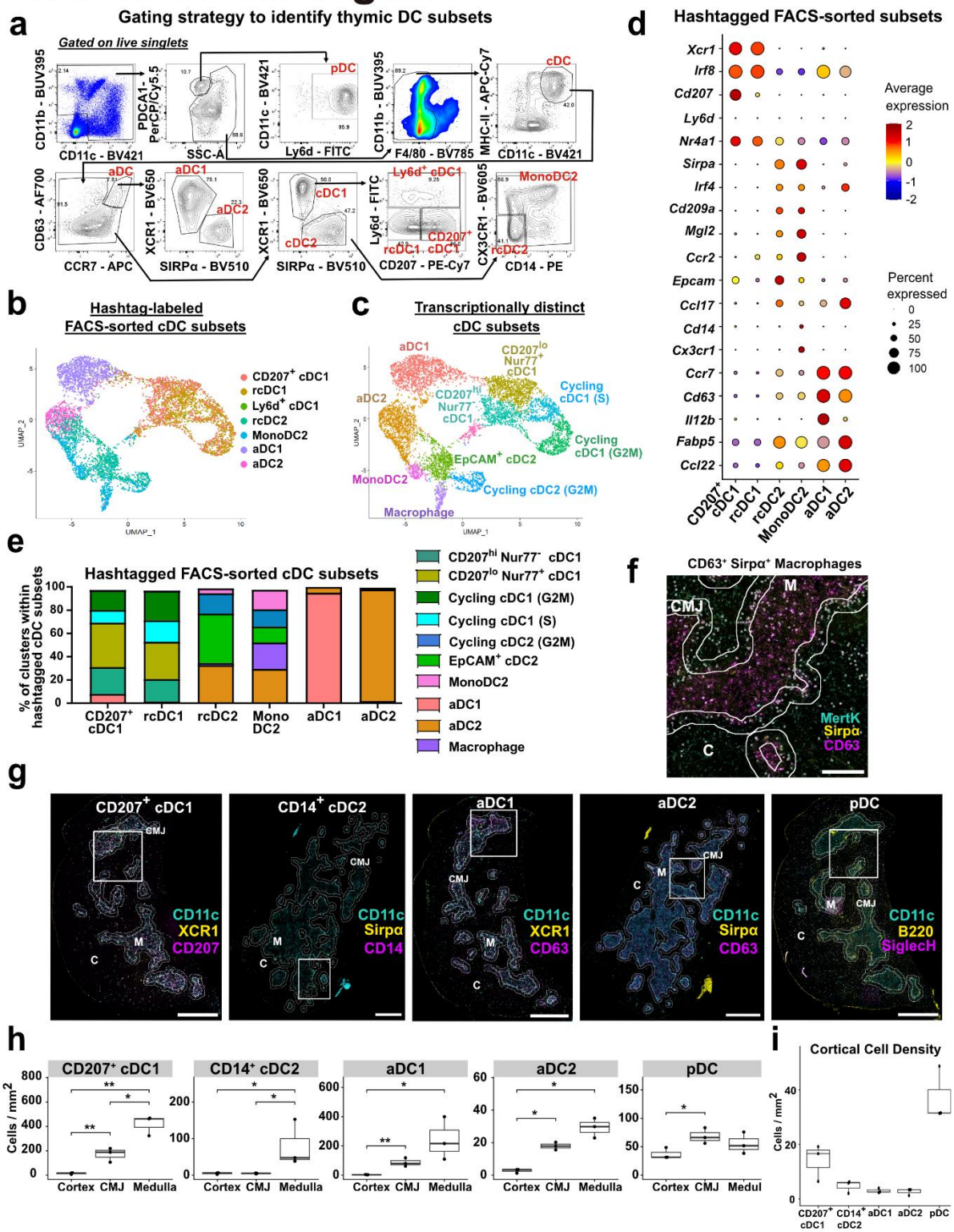

Extended Data Fig. 2. Identification of transcriptionally distinct cDC clusters and their correlation with FACS-sorted cDC subsets, related to Fig. 1.

(a) Flow cytometric gating strategy to identify distinct DC subsets shown in Fig. 1d. (b) UMAP visualization of scRNA-seq transcriptional data from pooled FACS-sorted cDC subsets, colored by their hashtag labels. (c) Same UMAP plot as (b), colored by transcriptionally distinct cDC clusters defined by the Seurat pipeline. (d) Dot plot showing normalized expression levels (z-score) of select genes associated with the hashtagged FACS-sorted cDC subsets. Expression is normalized per row (representing a gene) across different FACS-sorted cDC subsets. (e) Frequency of each transcriptionally distinct cDC cluster contained within the FACS-sorted hashtagged cDC subsets. (f) Immunofluorescence images of $MertK^+$ macrophages and $CD63^+SIRP\alpha^+MerTK^-$ aDC2s in thymic sections (representative of N=3 independent experiments). Centroids are placed over $CD63^+$ $SIRP\alpha^+$ cells that also express MertK: the frequency of MertK-expressing cells among $CD63^+SIRP\alpha^+$ myeloid cells was used to correct aDC2 densities from data as in (h). Scale bar, 250µm. Lines demarcate the cortex (C), medulla (M), and CMJ in the thymic sections. Centroids with 40% opacity were overlaid on the quantified cells. (g) Immunofluorescence of DC subsets (representative of N=3 independent experiments), identified by the indicated markers. White boxes indicate the regions of interest displayed in Fig. 1e. Scale bars, 1,000µm. (h) Quantification of cell densities of each of the indicated DC subsets in distinct anatomical regions of the thymus, based on histocytometry analyses of data as in (f-g). Data are compiled from N=3 independent experiments. Box plots represent mean ± SD. Statistical analysis was performed using Tukey's Honest Significant Difference test, where $*p<0.05$, $**p<0.01$. (i) Quantification of cortical cell densities of each of the indicated DC subsets, based on histocytometry analyses of data as in (f-g). Data are compiled from N=3 independent experiments. Box plots represent mean ± SD.

Extended Data Figure 3

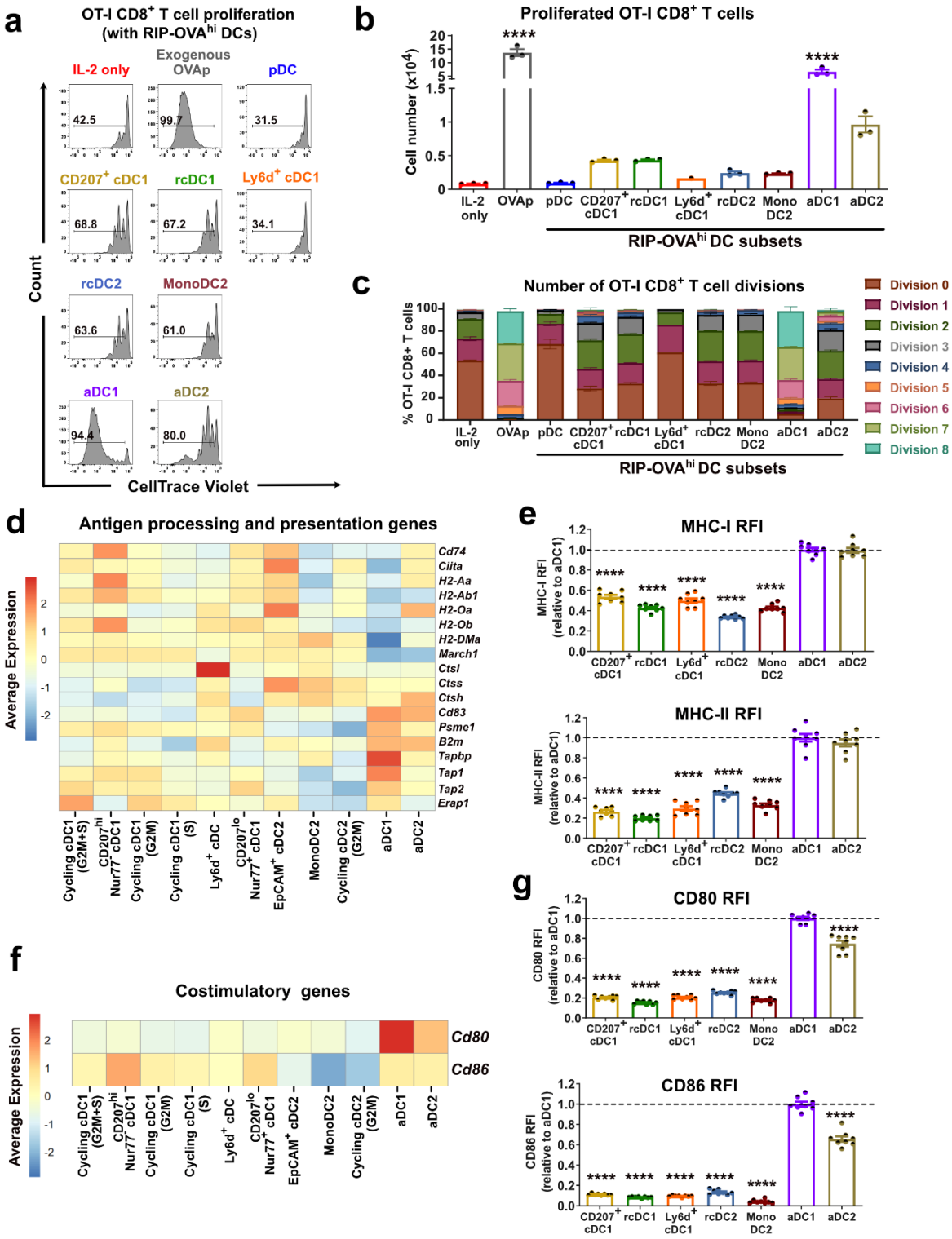

Extended Data Fig. 3. aDC1s, followed by aDC2s, are highly efficient at mTEC-derived antigen presentation on MHC-I and MHC-II, related to Fig. 2.

(a) Representative histograms showing the percentage of OT-I $CD8^+$ T cells that underwent at least 1 cell division after co-culture for 3.5 days with the specified DC subsets isolated from RIP-OVA^{hi} mice. OT-I $CD8^+$ T cells incubated only with IL-2 served as negative controls, while those co-cultured with OVA-pulsed splenocytes (50nM OVAp) served as positive controls. For (a-c), data are representative of 3 independent experiments.
(b) Quantification of OT-I $CD8^+$ T cells that underwent proliferation from the experiment described in (a). Bars represent mean ± SEM. Each dot represents a replicate well. Statistical analysis was performed using one-way ANOVA with Dunnett's multiple comparisons test, where ****$p<0.0001$. Significance is relative to "IL-2 only" control wells. (c) Modeling, based on data from the experiment in (a), of the frequency of OT-I $CD8^+$ T cells that underwent the indicated number of cell divisions. Bars represent mean ± SEM. (d, f) Heatmap displaying average normalized expression (z-score) of select (d) MHC-I and MHC-II antigen processing and presentation genes and (f) costimulatory genes in each cDC cluster from Fig. 1a. Expression is normalized per gene across different cDC clusters. (e, g) Relative cell-surface expression levels of (e) MHC-I and MHC-II, and (g) CD80 and CD86 proteins by cDC subsets, as determined by flow cytometry. Data are normalized to average MFI levels of aDC1s for each protein within an individual experiment. Data are compiled from N=3 independent experiments (n=8 mice). Bars represent mean ± SEM and symbols represent individual mice. Statistical analysis was performed using one-way ANOVA with Dunnett's multiple comparisons test, where ****$p<0.0001$. Significance is relative to the aDC1 subset.

Extended Data Figure 4

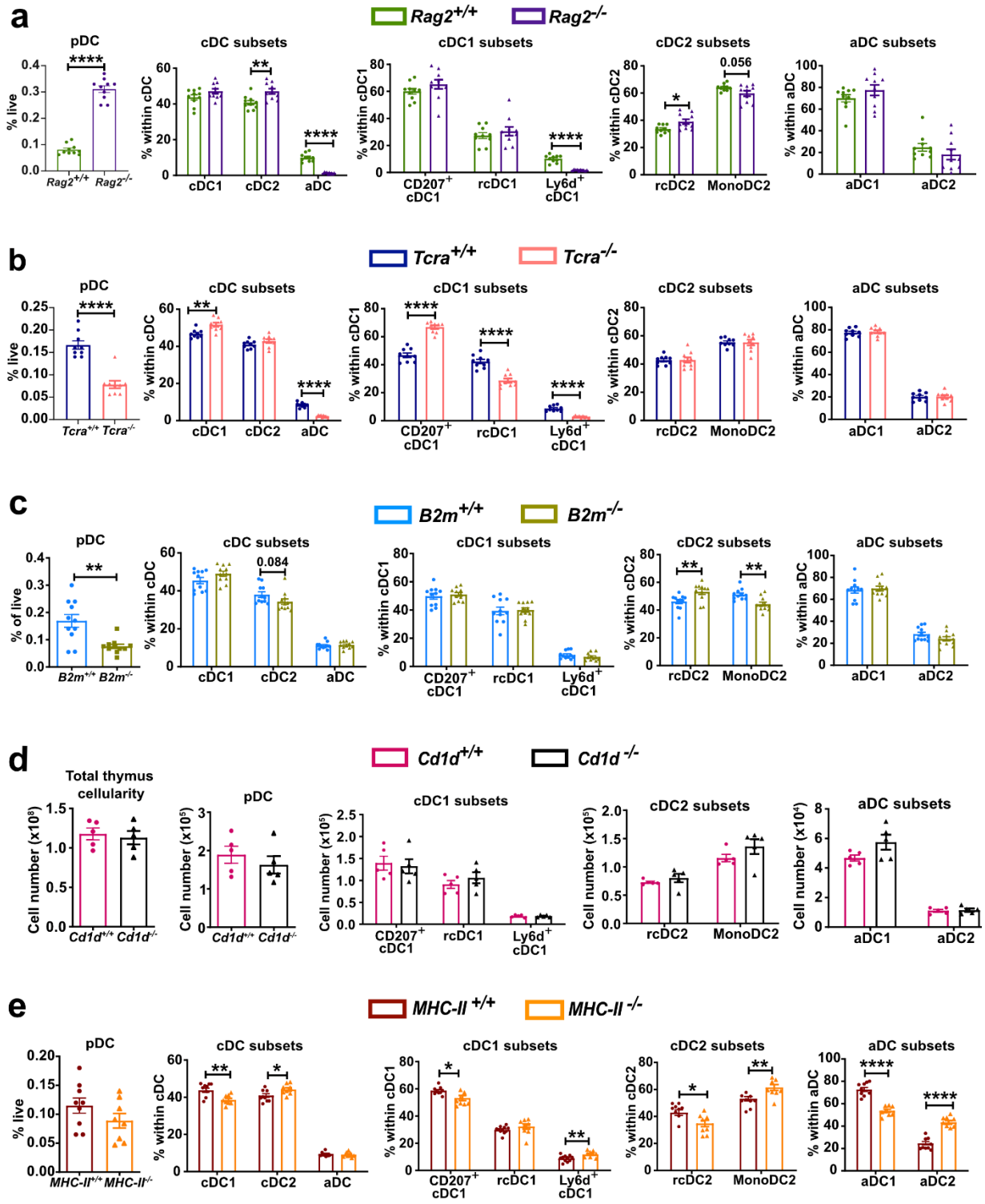

Extended Data Fig. 4. Thymic cDC1 and cDC2 homeostasis and activation depend on the presence of distinct thymocyte subsets, related to Fig. 3.

(a-c,e) Quantification of (left to right) frequencies of pDCs, total cDC subsets, cDC1 subsets, cDC2 subsets, and aDC subsets in the thymi of (a) *Rag2*$^{-/-}$, (b) *Tcra*$^{-/-}$, (c) *B2m*$^{-/-}$ and, (e) *MHC-II*$^{-/-}$ relative to littermate control mice. The population from which the frequencies were calculated is indicated on the respective Y-axes. (d) Quantification of (left to right) total thymus cellularity and cell numbers of pDCs, cDC1 subsets, cDC2 subsets, and aDC subsets of WT versus *Cd1d*$^{-/-}$ littermate mice. (a-e) Data are compiled from N=3-4 independent experiments (n=8-11 mice). Bars represent mean ± SEM and symbols represent individual mice. Statistical analysis was performed using unpaired Student *t*-test where *p<0.05, ** p<0.01, ***p<0.001, ****p<0.0001.

Extended Data Figure 5

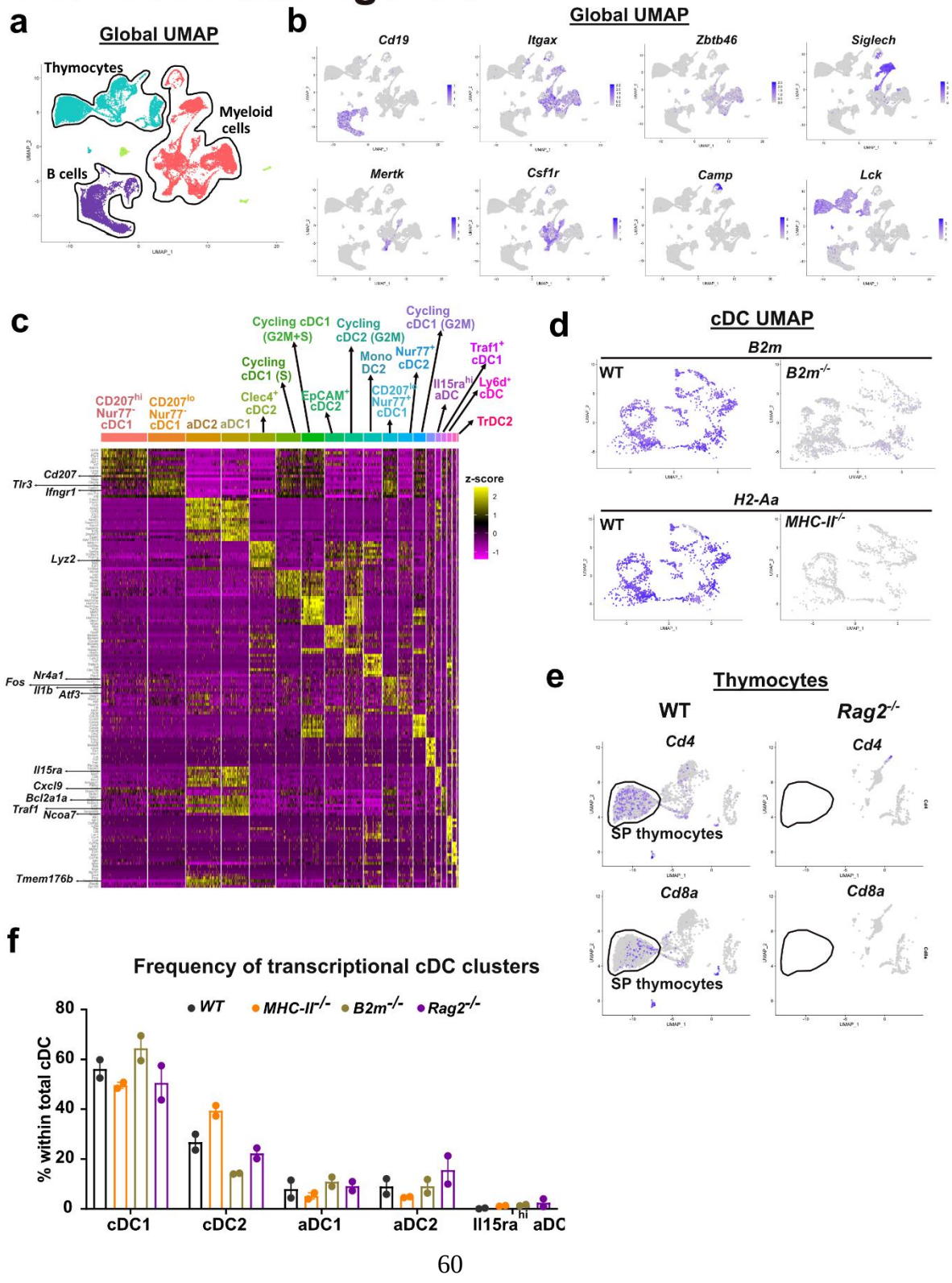

Extended Data Fig. 5. Transcriptional profiling of thymic HAPCS in mice devoid of distinct thymocyte subsets reveals the impact on cellular transcriptomes and frequencies, related to Fig. 4.

(a) Merged UMAP visualization of 34,750 cells depicting major cell continents in WT, *MHC-II*$^{-/-}$, *B2m*$^{-/-}$ and *Rag2*$^{-/-}$ HAPC scRNA-seq datasets. Data are compiled from N=2 independent experiments (n=2 mice). (b) Feature plots displaying expression levels of select genes associated with distinct HAPC subtypes – B cells (*Cd19*), cDC (*Itgax, zbtb46*), pDC (*Siglech, Itgax*), Macrophages and Monocytes (*MertK, Csf1r*) and granulocytes (*Camp*). Residual thymocytes included in the sorted cells were identified by *Lck* expression. (c) Heatmap displaying normalized expression of the top 10 enriched genes in each transcriptionally distinct cDC cluster from Fig. 4a. (d) Feature plots showing scRNA-seq expression levels of (top) *B2m* transcripts in WT versus *B2m*$^{-/-}$ cDCs and (bottom) *H2-Aa* transcripts in WT versus *MHC-II*$^{-/-}$ cDCs overlaid on the UMAP visualization from Fig. 4a. (e) Feature plots showing expression levels of *Cd4* and *Cd8a* transcripts in thymocytes from WT versus *Rag2*$^{-/-}$ mice overlaid on the UMAP visualization in (a). (f) Quantification of the frequencies of cDC1, cDC2, aDC1, aDC2, and Il15ra^{hi} aDC subsets identified in Fig. 4a from scRNA-seq transcriptional profiling of thymic DCs in the four indicated genotypes. Data are compiled from 2 independent experiments per genotype (n=2 mice). Bars represent mean ± SEM and symbols represent individual mice.

Extended Data Figure 6

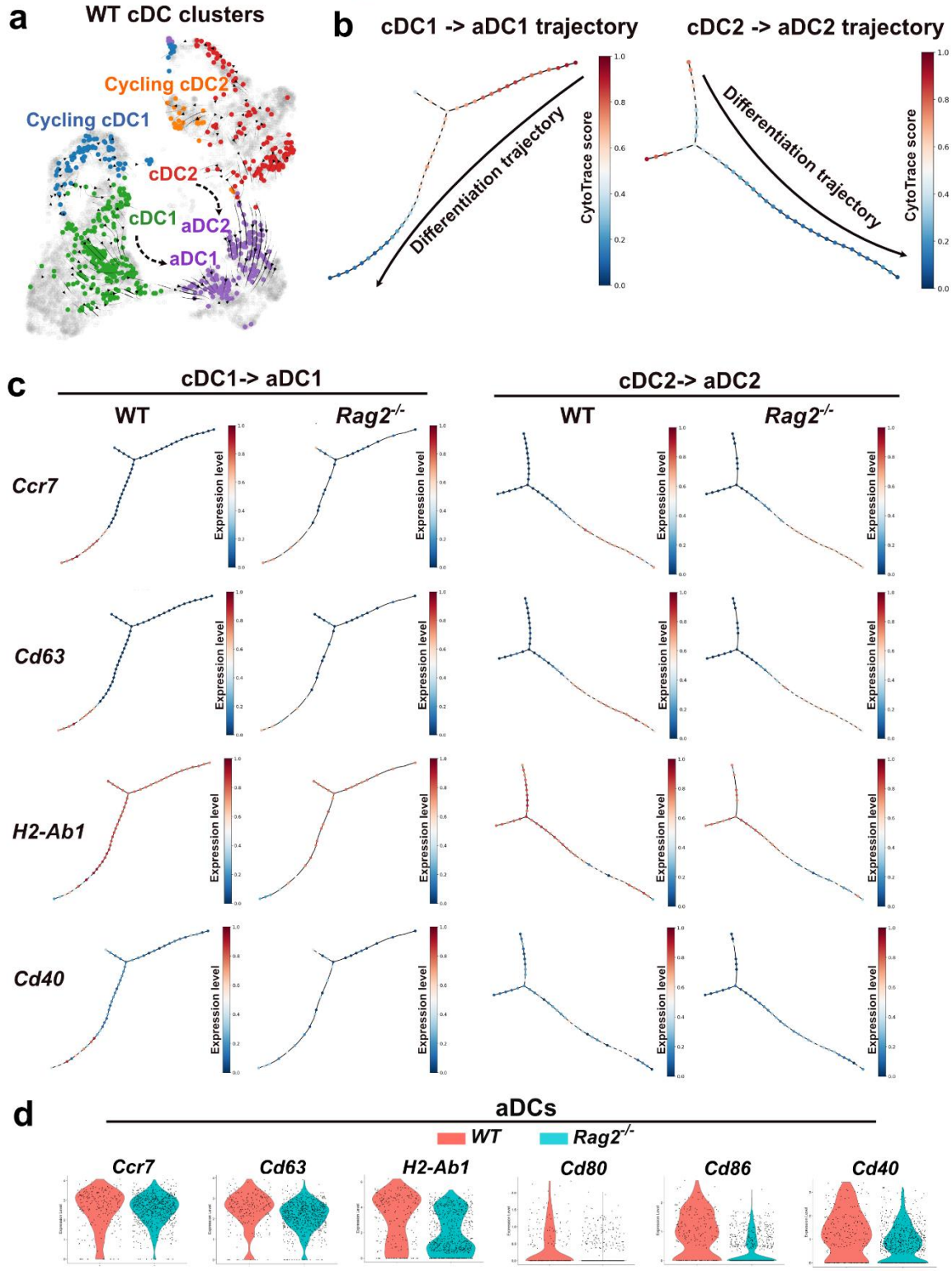

Extended Data Fig. 6. SP thymocytes are necessary for full cDC activation, related to Fig. 5.

(a) RNA velocity analysis with arrows showing relative transition probabilities derived from ratio calculations of unspliced over spliced transcripts (cDCs -> aDCs). (b) p-Creode analysis depicting cell-state transition trajectories for (left) cDC1 and (right) cDC2 transcriptional subsets. The topology was constructed with hierarchical placement, which connects the two transcriptionally closest end-states with path nodes. Overlay represents CytoTrace score to indicate cells with a high degree of stemness and transcriptional diversity (score closer to 1) versus those with a low degree of stemness, indicative of a more differentiated transcriptional state (score closer to 0). (c) p-Creode (left) cDC1 and (right) cDC2 differentiation trajectories from WT and *Rag2*$^{-/-}$ scRNA-seq datasets overlaid with normalized expression values of select genes associated with cDC activation and licensing. (d) Violin plots showing normalized expression levels of the indicated genes, associated with DC activation or costimulation of T cells, in WT versus *Rag2*$^{-/-}$ aDCs (combined aDC1, aDC2, and Il15ra^{hi} aDC clusters).

Extended Data Figure 7

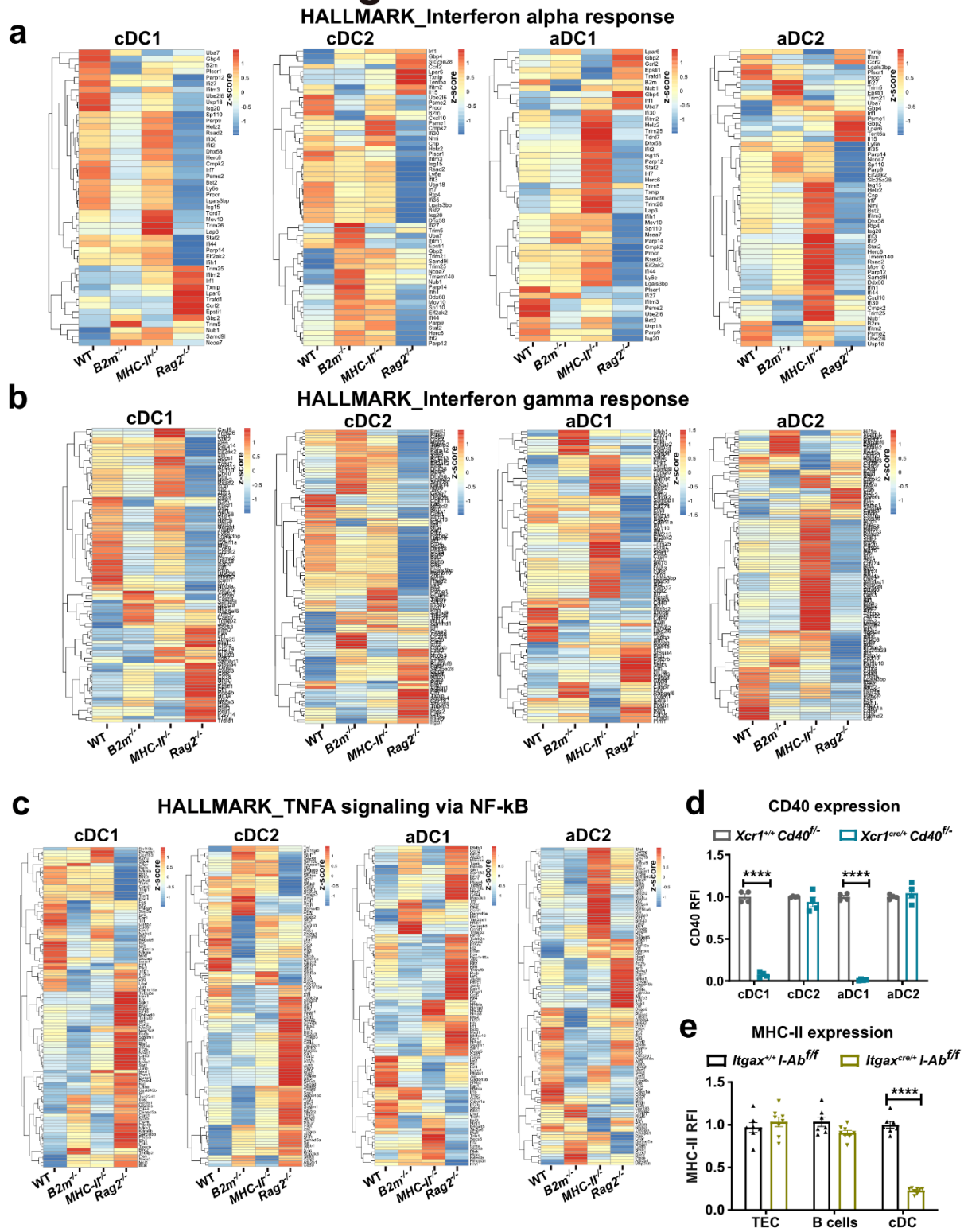

Extended Data Fig. 7. CD8SP thymocytes promote expression of genes associated with interferon signaling in DCs, while DCs activated in the absence of SP thymocytes express elevated levels of genes associated with canonical NF-kB signaling, related to Fig. 5.

(a-c) Heatmaps show normalized expression (z-score) of genes associated with the indicated pathways in cDC1s, cDC2s, aDC1s and aDC2s. Genes shown represent the union of differentially regulated genes identified via tradeSeq analysis along the p-Creode cDC1 and cDC2 differentiation trajectories from pairwise WT versus KO comparisons (Fig. 5c-d). Pathways were identified via gene enrichment analysis of the differentially regulated genes along the cDC1/cDC2 trajectories, carried out using WebgestaltR with pathways from KEGG and MSigDB databases. (d) CD40 RFI levels on cDC1, cDC2, aDC1, and aDC2 subsets from *Xcr1*$^{+/+}$ *Cd40*$^{f/-}$ versus *Xcr1*$^{cre/+}$ *Cd40*$^{f/-}$ littermate mice. Data are normalized to average MFI levels of the respective subset in *Xcr1*$^{+/+}$ *Cd40*$^{f/-}$ control mice per experimental repeat. (e) MHC-II RFI levels on CD11c^{+} cDCs, CD45^{-}EpCAM^{+} MHCII^{+} thymic epithelial cells (TECs), and CD45^{+}CD19^{+}MHC-II^{+} B cells from *Itgax*$^{+/+}$ *I-Ab*$^{f/f}$ versus *Itgax*$^{cre/+}$ *I-Ab*$^{f/f}$ littermate mice. Data are normalized to average MFI levels of the respective subset in *Itgax*$^{+/+}$ *I-Ab*$^{f/f}$ control mice per experimental repeat. (d-e) Bars represent mean ± SEM and symbols represent individual mice. Data are compiled from N=2-3 independent experiments (n=4-8 mice). Statistical analysis was performed using unpaired Student *t*-test where ****$p<0.0001$.